Exploring the sensitivity to non-standard neutrino interactions of NaI and cryogenic CsI detectors at the Spallation Neutron Source

Sabya Sachi Chatterjee[1,2,*] Stéphane Lavignac[2,†] O. G. Miranda[3,‡] and G. Sanchez Garcia[4,§]

[1]*Institut für Astroteilchenphysik, Karlsruher Institut für Technologie (KIT), 76021 Karlsruhe, Germany*
[2]*Institut de Physique Théorique, Université Paris Saclay, CNRS, CEA, F-91191 Gif-sur-Yvette, France*
[3]*Departamento de Física, Centro de Investigación y de Estudios Avanzados del IPN,*
Apartado Postal 14-740 07000, Ciudad de Mexico, Mexico
[4]*Instituto de Física Corpuscular (CSIC-Universitat de València),*
Parc Científic UV, C/ Catedràtico José Beltrán, 2, 46980 Paterna, Spain

After the first observation of coherent elastic neutrino-nucleus scattering (CEνNS) by the COHERENT Collaboration, many efforts are being made to improve the measurement of this process, making it possible to constrain new physics in the neutrino sector. In this paper, we study the sensitivity to non-standard interactions (NSIs) and generalized neutrino interactions of two experimental setups at the Spallation Neutron Source at Oak Ridge National Laboratory: a NaI detector with characteristics similar to the one that is currently being deployed there and a cryogenic CsI detector proposed at the same facility. We show that a combined analysis of the data from these detectors, whose target nuclei have significantly different proton-to-neutron ratios, could help to partially break the parameter degeneracies arising from the interference between the Standard Model and NSI contributions to the CEνNS cross section, as well as between different NSI parameters. By contrast, only a slight improvement over the current CsI constraints is expected for parameters that do not interfere with the SM contribution.

I. INTRODUCTION

Coherent elastic neutrino-nucleus scattering (CEνNS) [1] is a privileged process to probe new physics in the neutrino sector. So far, the only measurements of CEνNS have been done at the Spallation Neutron Source (SNS) at Oak Ridge National Laboratory, USA, by the COHERENT Collaboration. The first observation of this process was performed with a CsI detector [2,3]. Another detector, with liquid argon as a target, was subsequently used by the COHERENT Collaboration [4]. These measurements allowed to test the Standard Model at low energy [5], to constrain the neutron root mean square *(rms)* radius of cesium, iodine [6] and argon [7], and to probe various possible manifestations of physics beyond the Standard Model, such as non-standard neutrino

interactions (NSIs) [8–11], generalized neutrino interactions (GNIs) [10,12–15], neutrino electromagnetic properties [16–18], new light gauge bosons [14,19–22], and sterile neutrinos [10,23,24], among others. Future CEνNS experiments at spallation neutron sources [25–27] or nuclear reactors [28–31] will provide more data using different target materials. Particularly interesting is the possibility to disentangle new physics from Standard Model parameters using the interplay between experiments with different neutrino sources [32,33]. In addition, using nuclear targets with different proportions of protons and neutrons can help to reduce the parameter degeneracies arising from the interference between standard and non-standard contributions to CEνNS, e.g., in the presence of NSIs [8].

A broad class of new physics models predict low-energy effects in the lepton sector that can effectively be described in terms of NSIs or GNIs [34–37]. CEνNS is an excellent process to test such new physics effects and to resolve the degeneracies that appear in the interpretation of neutrino oscillation data in the presence of NSIs [38,39]. However, the possibility of constraining NSI parameters with CEνNS is limited by the possible cancellations between standard and non-standard contributions to the cross section, as well as between different NSI couplings. It is therefore crucial to perform CEνNS measurements

---

[*]Contact author: sabya.chatterjee@kit.edu
[†]Contact author: stephane.lavignac@ipht.fr
[‡]Contact author: omar.miranda@cinvestav.mx
[§]Contact author: gsanchez@ific.uv.es

with different neutrino sources and targets in order to break these degeneracies [8,9,26,39–41].

In this work, we study the expected sensitivities to non-standard and generalized neutrino interactions of two experimental setups at the Spallation Neutron Source: a NaI detector with characteristics similar to the one that is currently being deployed there [42], expected to be sensitive only to sodium recoils [43], and a cryogenic CsI detector proposed at the same facility [44]. The target nuclei of these detectors have significantly different proton-to-neutron ratios ($p/n \simeq 0.71$, 0.72 for cesium and iodine, and $p/n \simeq 0.92$ for sodium). As we will show, this important feature makes a combined analysis of the data from both detectors particularly efficient at breaking degeneracies involving flavor-diagonal NSI parameters. For generalized neutrino interactions and flavor off diagonal NSIs, whose contribution to the CEνNS cross section does not interfere with the SM one, no significant improvement over the constraints extracted from the current CsI data is expected.

The paper is structured as follows. In Sec. II, we discuss the NSI and GNI contributions to the CEνNS cross section. In Sec. III, we present the experimental setup at the SNS and the characteristics of the current CsI and future NaI and cryogenic CsI detectors. Section IV details our analysis procedure. The expected sensivities of the future detectors, and of their combination, to NSI and GNI parameters are presented in Sec. V, and compared with the current CsI constraints. Finally, we present our conclusions in Sec. VI.

II. THEORETICAL FRAMEWORK

In this section, we discuss the necessary tools to probe GNI through CEνNS measurements. We begin by introducing the SM prediction for the CEνNS cross section, and then we discuss how this cross section is modified when GNI parameters are introduced.

A. The standard CEνNS cross section

In the Standard Model, the cross section for the coherent elastic scattering of a neutrino or antineutrino of flavor α ($\alpha = e, \mu, \tau$) and energy E_ν off a nucleus with Z protons, N neutrons and mass M is given [up to subleading terms of order T/E_ν, $(T/E_\nu)^2$ [8] and small radiative corrections [45]] by [1]

$$\frac{\mathrm{d}\sigma}{\mathrm{d}T}(E_\nu, T) = \frac{G_F^2 M}{\pi}\left(1 - \frac{MT}{2E_\nu^2}\right)F^2(|\vec{q}|^2)Q_{W,\alpha}^2, \quad (1)$$

where G_F is the Fermi constant, T the nuclear recoil energy, $F(|\vec{q}|^2)$ the form factor of the nucleon distribution in the nucleus [46] (assumed to be the same for protons and neutrons) evaluated at the transferred three-momentum $|\vec{q}| \simeq \sqrt{2MT}$, and

$$Q_{W,\alpha} = Zg_V^p + Ng_V^n, \quad (2)$$

with $g_V^p = \frac{1}{2} - 2\sin^2\theta_W$ and $g_V^n = -\frac{1}{2}$, is the weak nuclear charge. Since $|\vec{q}|$ is typically very small in CEνNS, the value of the weak mixing angle is taken at zero momentum transfer ($\sin^2\theta_W = 0.23867$ [47,48]).

The form factor $F(|\vec{q}|^2)$ describes the loss of coherence of the scattering when $|\vec{q}| \gtrsim R^{-1}$, where R is the nucleon radius. Following the COHERENT Collaboration, we use the Klein-Nystrand parametrization for the nuclear form factor [49],

$$F(|\vec{q}|^2) = 3\frac{j_1(|\vec{q}|R_A)}{|\vec{q}|R_A}\left(\frac{1}{1 + |\vec{q}|^2 a_k^2}\right), \quad (3)$$

where $j_1(x) = (\sin x - x\cos x)/x^2$ is the spherical Bessel function of order one, $a_k = 0.9$ fm and $R_A = 1.23A^{1/3}$ fm is the nuclear radius, with A the total number of nucleons of the target nucleus.

B. Non-standard and generalized neutrino interactions

The CEνNS cross section is potentially affected by any interaction between neutrinos and quarks that may be generated by new physics beyond the Standard Model. The simplest example of such interactions are the so-called (neutral-current) non-standard neutrino interactions (NC-NSIs, or NSIs for short), whose phenomenology has been widely studied (see, e.g., the reviews [35–37,50] and references therein). They are usually parametrized as

$$\mathcal{L}_{\text{NC-NSI}} = -\sqrt{2}G_F\{\varepsilon_{\alpha\beta}^{fV}(\bar{\nu}_\alpha\gamma^\mu P_L\nu_\beta)(\bar{f}\gamma_\mu f) + \varepsilon_{\alpha\beta}^{fA}(\bar{\nu}_\alpha\gamma^\mu P_L\nu_\beta)(\bar{f}\gamma_\mu\gamma^5 f)\}, \quad (4)$$

where $\alpha, \beta = e, \mu, \tau$ denote the neutrino flavors, $f = u, d$ label the up and down quarks (we omit the leptonic NSIs, $f = e$, as they do not contribute to CEνNS), summation over α, β, and f is implicit, and $\varepsilon_{\alpha\beta}^{fV}$, $\varepsilon_{\alpha\beta}^{fA}$ are the vector and axial-vector NSI couplings, respectively. In this paper, we do not consider the axial-vector NSIs, because their contribution to the CEνNS cross section depends on the nuclear spin and is therefore negligible for heavy nuclei [13], similarly to the contribution of the neutral current axial couplings in the SM [8,51].

Non-standard neutrino-quark interactions can have a more general Lorentz structure than the one of Eq. (4). Namely, one may also consider scalar, pseudoscalar and tensor couplings,[1] usually dubbed "generalized neutrino interactions" (GNIs) in the literature [13,34,53],

---

[1]The tensor operators $(\bar{\nu}_\alpha\sigma^{\mu\nu}P_L\nu_\beta)(\bar{q}\sigma_{\mu\nu}P_R q)$ vanish by Lorentz symmetry [52], hence do not appear in Eq. (5).

$$\mathcal{L}_{\text{GNI}} = -\sqrt{2}G_F\{\varepsilon_{\alpha\beta}^{qS}(\bar{\nu}_\alpha P_L \nu_\beta)(\bar{q}q) + \varepsilon_{\alpha\beta}^{qP}(\bar{\nu}_\alpha P_L \nu_\beta)(\bar{q}\gamma^5 q)$$
$$+ \varepsilon_{\alpha\beta}^{qT}(\bar{\nu}_\alpha \sigma^{\mu\nu}P_L \nu_\beta)(\bar{q}\sigma_{\mu\nu}P_L q)\} + \text{H.c.,} \tag{5}$$

where $\sigma^{\mu\nu} = \frac{i}{2}[\gamma^\mu, \gamma^\nu]$ and $q = u,\ d$. Generally, NSIs are also included in the GNI Lagrangian. In the following, we will refer to $\varepsilon_{\alpha\beta}^{qS}$, $\varepsilon_{\alpha\beta}^{qV}$, and $\varepsilon_{\alpha\beta}^{qT}$ as scalar, vector, and tensor couplings, respectively (we will not consider pseudoscalar interactions, which give a negligible contribution to CEνNS [13,34]). Note that Hermiticity of the Lagrangian implies $\varepsilon_{\beta\alpha}^{qV} = (\varepsilon_{\alpha\beta}^{qV})^*$, while the matrices of scalar and tensor couplings do not have any particular symmetry property if neutrinos are Dirac fermions. If they are Majorana fermions, instead, one has $\varepsilon_{\beta\alpha}^{qS} = \varepsilon_{\alpha\beta}^{qS}$ and $\varepsilon_{\beta\alpha}^{qT} = -\varepsilon_{\alpha\beta}^{qT}$ (in particular, flavor-diagonal tensor couplings vanish for Majorana neutrinos).

In the presence of scalar, vector, and tensor non-standard neutrino interactions, the differential CEνNS cross section (1) for an incident neutrino of flavor α is modified to [34]

$$\frac{d\sigma}{dT}(E_\nu, T) = \frac{G_F^2 M}{\pi}F^2(|\vec{q}|^2)\sum_{\beta=e,\mu,\tau}\left[|C_{\beta\alpha}^S|^2\frac{MT}{8E_\nu^2} + |C_{\beta\alpha}^V\right.$$
$$\left. + Q_{W,\alpha}\delta_{\alpha\beta})|^2\left(1 - \frac{MT}{2E_\nu^2}\right)\right.$$
$$\left. + 2|C_{\beta\alpha}^T|^2\left(1 - \frac{MT}{4E_\nu^2}\right)\right], \tag{6}$$

where subleading terms of order $T/E_\nu \ll MT/E_\nu^2$ have been omitted.[2] For an incident antineutrino of flavor α, one should replace $C_{\beta\alpha}^S \to C_{\alpha\beta}^S$, $C_{\beta\alpha}^V \to C_{\alpha\beta}^V$, and $C_{\beta\alpha}^T \to C_{\alpha\beta}^T$ in Eq. (6). The SM contribution is contained in the weak nuclear charge $Q_{W,\alpha}$, given by Eq. (2), while the non-standard contributions are encapsulated in the coefficients $C_{\alpha\beta}^S$, $C_{\alpha\beta}^V$, and $C_{\alpha\beta}^T$, which are given by [13]

$$C_{\alpha\beta}^S = \sum_{q=u,d}\left(Z\frac{m_p}{m_q}f_q^p + N\frac{m_n}{m_q}f_q^n\right)\varepsilon_{\alpha\beta}^{qS}, \tag{7}$$

$$C_{\alpha\beta}^V = (2Z + N)\varepsilon_{\alpha\beta}^{uV} + (Z + 2N)\varepsilon_{\alpha\beta}^{dV}, \tag{8}$$

$$C_{\alpha\beta}^T = \sum_{q=u,d}(Z\delta_q^p + N\delta_q^n)\varepsilon_{\alpha\beta}^{qT}. \tag{9}$$

For the numerical coefficients appearing in Eqs. (7) and (9), we adopt the values given in Refs. [54,55], respectively,

$$f_u^p = 0.0208, \quad f_d^p = 0.0411, \quad f_u^n = 0.0189, \quad f_d^n = 0.0451, \tag{10}$$

$$\delta_u^p = 0.792, \quad \delta_d^p = -0.194, \quad \delta_u^n = -0.194, \quad \delta_d^n = 0.792. \tag{11}$$

As for quark masses, we use the central values given by the Particle Data Group [48], $m_u = 2.2$ MeV and $m_d = 4.7$ MeV. Given the large uncertainties associated with the light quark masses and with f_q^N and δ_q^N, many authors provide constraints on the coefficients $C_{\alpha\beta}^S$ and $C_{\alpha\beta}^T$ rather than on the Lagragian parameters $\varepsilon_{\alpha\beta}^{qS}$ and $\varepsilon_{\alpha\beta}^{qT}$. In this paper, we choose instead to constrain the Lagrangian parameters for fixed values of m_q, f_q^N, and δ_q^N. It is straightforward to translate the current bounds and future sensitivity estimates on $\varepsilon_{\alpha\beta}^{qS}$ and $\varepsilon_{\alpha\beta}^{qT}$ presented in the next sections into constraints on $C_{\alpha\beta}^S$ and $C_{\alpha\beta}^T$.

Other authors, e.g., in Refs. [10,13,34,56,57], use the symbols C_S^q, C_V^q, C_T^q instead of ε^{qS}, ε^{qV}, ε^{qT} in Eqs. (7) to (9), with depending on the normalization convention either $C_V^q = \varepsilon^{qV}$ [57] [with the CEνNS cross section given by Eq. (6)] or $C_V^q = 2\varepsilon^{qV}$ [10,13,34,56] [in which case, one should replace $C_{\alpha\beta}^V$ by $\frac{1}{2}C_{\alpha\beta}^V$ in Eq. (6)].

III. EXPERIMENTAL SETUP AND DETECTORS

In this section, we describe the SNS neutrino beam and the main characteristics of the three detectors considered in this paper: the current CsI detector used by the COHERENT Collaboration, a future NaI detector similar to the one under deployment at the SNS [42], and a cryogenic CsI detector proposed by the same collaboration [44].

A. Neutrino beam and predicted number of CEνNS events

At the SNS, the neutrinos used for CEνNS measurements arise from the decays at rest of the π^+ produced, together with neutrons and π^-'s, from the collision of high-energy protons on a mercury target (in which the π^- are absorbed before decaying). The SNS neutrino beam therefore consists of three components: a prompt, monoenergetic ν_μ component produced in the two-body decays of stopped positively charged pions ($\pi^+ \to \mu^+ + \nu_\mu$), and two delayed $\bar{\nu}_\mu$ and ν_e components arising from the subsequent decays at rest of the antimuons ($\mu^+ \to e^+ + \bar{\nu}_\mu + \nu_e$). These contributions can be analytically computed and are given by

$$\frac{dN_{\nu_\mu}}{dE_\nu} = \xi\delta\left(E_\nu - \frac{m_\pi^2 - m_\mu^2}{2m_\pi}\right), \tag{12}$$

---

[2]In particular, we omit a scalar-tensor interference term in Eq. (6), which is proportional to T/E_ν and whose sign is different for neutrinos and antineutrinos [34].

$$\frac{dN_{\bar{\nu}_\mu}}{dE_\nu} = \xi \frac{64E_\nu^2}{m_\mu^3}\left(\frac{3}{4} - \frac{E_\nu}{m_\mu}\right),$$ (13)

$$\frac{dN_{\nu_e}}{dE_\nu} = \xi \frac{192E_\nu^2}{m_\mu^3}\left(\frac{1}{2} - \frac{E_\nu}{m_\mu}\right),$$ (14)

where E_ν is the neutrino energy and $\xi = rN_{\text{POT}}/4\pi L^2$ is a normalization factor that depends on several experimental features: N_{POT}, the number of protons on target (POT) throughout the operation time; r, the number of neutrinos per flavor produced by each POT; and L, the distance between the source and the detector.

Given the neutrino flux, the predicted number of CEνNS events in the nuclear recoil energy bin $[T_i, T_{i+1}]$ is given by, for a target material consisting of a single nucleus with mass M,

$$N_i^{th} = \mathcal{N} \int_{T_i}^{T_{i+1}} A(T)dT \int_0^{T'_{\max}} \mathcal{R}(T, T')dT'$$
$$\times \sum_{\nu=\nu_e,\nu_\mu,\bar{\nu}_\mu} \int_{E_{\min}(T')}^{E_{\max}} dE_\nu \frac{dN_\nu}{dE_\nu}(E_\nu)\frac{d\sigma}{dT'}(E_\nu, T'),$$ (15)

where $d\sigma/dT$ is the relevant CEνNS cross section, given by Eqs. (1) or (6), and $\mathcal{N} = N_A M_{\text{det}}/M_{\text{mol}}$ is the number of nuclei in the detector, which is computed from the detector mass M_{det} and the molar mass of the nucleus M_{mol}, with N_A the Avogadro constant. The lower limit of the integral over E_ν is the minimal neutrino energy that can induce a nuclear recoil of energy T', $E_{\min}(T') = \sqrt{MT'/2}$, while the upper limit $E_{\max}$ is the maximum neutrino energy, which for the SNS beam is 52.8 MeV. Notice that Eq. (15) depends on both the real (T') and the reconstructed (T) nuclear recoil energies, with $\mathcal{R}(T, T')$ the smearing function, which may be different for each detector, and the upper limit of the integral over T' is the maximal nuclear recoil energy that can be induced by a neutrino from the beam, $T'_{\max} = 2E_{\max}^2/M$. Finally, $A(T)$ is an acceptance function, which also depends on the detector. If the target material consists of two nuclei, as is the case for the CsI and NaI detectors, the total number of CEνNS events is the sum of the numbers of neutrino scatterings on each nucleus, computed separately from Eq. (15) with the appropriate values of M and M_{mol}.

When the timing information of the experiment is available, one can also bin the data in time intervals. In this case, the predicted number of events in the nuclear recoil energy bin i and time bin j is given by

$$N_{ij}^{th} = \sum_{\nu=\nu_e,\nu_\mu,\bar{\nu}_\mu} N_{\nu,i}^{th} \int_{t_j}^{t_{j+1}} f_\nu(t)\varepsilon_t(t)dt,$$ (16)

where $N_{\nu,i}^{th}$ is the predicted number of CEνNS events induced by the component ν ($\nu = \nu_e, \nu_\mu, \bar{\nu}_\mu$) of the neutrino

TABLE I. Main properties of the target nuclei used in the detectors considered in this work: number of protons (Z) and neutrons (N), proton-to-neutron ratio (Z/N) and mass in atomic units (M).

Target nucleus	Z	N	Z/N	M (a.m.u)
Cs	55	78	0.71	132.91
I	53	74	0.72	126.90
Na	11	12	0.92	22.99

flux in the nuclear recoil energy bin $[T_i, T_{i+1}]$, $f_\nu(t)$ is the time distribution of the neutrino flux component ν taken from Ref. [58], and $\varepsilon(t)$ is the timing efficiency provided in Ref. [3]. To compute $N_{\nu,i}^{th}$, we use Eq. (15) without performing the sum over the contributions of the three components of the neutrino flux.

In our analysis, we use the data of the current CsI detector of the COHERENT Collaboration, as well as the expected future data from a NaI and cryogenic CsI detectors at the SNS. The main characteristics of these detectors are described in the following subsections, and the relevant properties of their target nuclei are given in Table I.

B. Current CsI detector

The COHERENT Collaboration performed CEνNS measurements with a 14.6 kg CsI detector located at 19.3 m from the neutrino source [3]. The accumulated data correspond to $N_{\text{POT}} = 3.198 \times 10^{23}$, with a number of neutrinos per flavor of $r = 0.0848$ [3]. These numbers are used to compute the neutrino fluxes though Eqs. (12)–(14). Following the COHERENT Collaboration, we take the smearing function $\mathcal{R}(T, T')$ in Eq. (15) to be the gamma function given in Ref. [3] (we refer the reader to Ref. [10] for details about the smearing procedure). Finally, we take into account the timing information provided by the COHERENT Collaboration in our analysis and use Eq. (16) to compute the predicted number of events in each recoil energy and time bin. In this way, we obtain an event spectrum in energy and time that reproduces the one presented in the Appendix of Ref. [10].

C. Future NaI detector

The complete program of the COHERENT Collaboration includes a NaI-based detector comprising several modules, each consisting of individual 7.7 kg NaI crystals [25]. In its final design, this detector is expected to have up to seven modules, each containing 63 crystals, giving a total mass $M_{\text{det}} = 3395.7$ kg, which we shall consider in this work. The detector is expected to be located at a distance $L = 22$ m from the neutrino source [25]. By the time this detector is scheduled to be fully deployed, the SNS is expected to operate at an average power of 2 MW with a proton energy $E_p = 1.3$ GeV, for which a value of $r = 0.13$
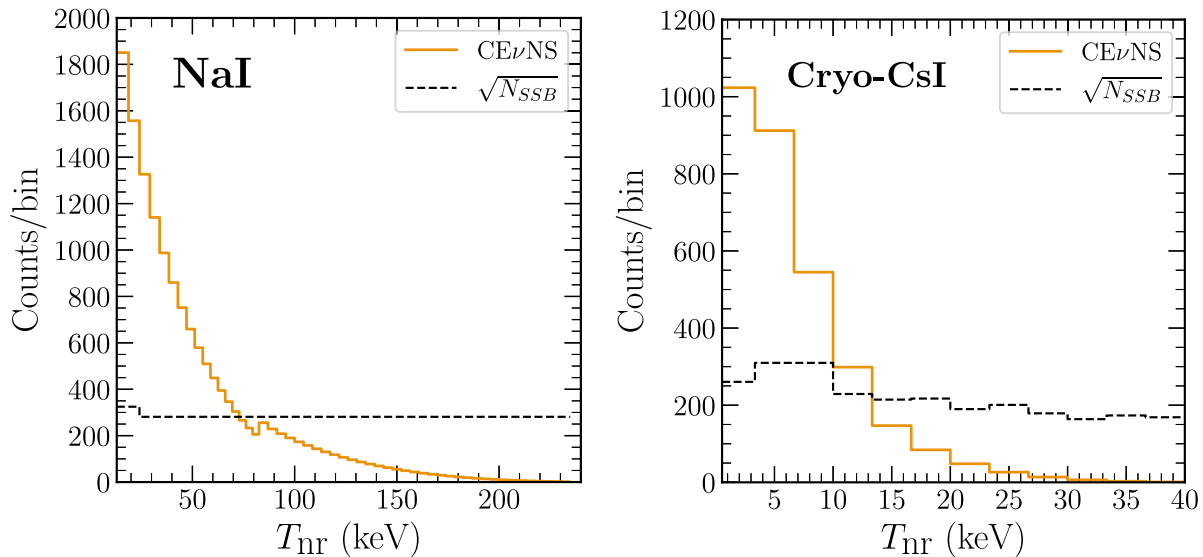
FIG. 1.   Projected numbers of signal and background events in the SM as a function of the reconstructed nuclear recoil energy for the future NaI (left) and Cryo-CsI (right) detectors considered in this paper, assuming 3 years of data taking. The signal spectra include the contributions of the three components of the SNS neutrino beam (ν_e, ν_μ, and $\bar{\nu}_\mu$). The expected steady-state background is represented by the black dashed curve, which shows the square root of the actual number of background events for NaI.

is predicted in Ref. [59]. Under these assumptions, we get a total number of protons on target (POT) of 1.73×10^{23} per calendar year of data taking, assuming $\simeq 5000$ hours (208.3 days) of operation per year. In this work, we consider 3 years of data taking with the SNS operating at a beam power of 2 MW with $E_p = 1.3$ GeV, giving a total number of protons on target $N_{\mathrm{POT}} = 5.2 \times 10^{23}$.

Even though the NaI molecule contains two nuclei, the detector will be only sensitive to Na recoils. Indeed, due to a low quenching factor QF(I) $\leq 8\%$, the nuclear recoil energy threshold for iodine is such that only a tiny fraction of the iodine-induced CEνNS events can be detected.[3] We can therefore safely neglect them. To compute the expected number of (Na-induced) CEνNS events in the future NaI detector, we assume a conservative constant acceptance of 80% and a Gaussian smearing function $\mathcal{R}(T, T')$ with an energy-dependent resolution $\sigma(T) = \eta\sqrt{TT_{th}}$, where[4] $\eta = 0.14$ and $T_{th} = 13\mathrm{keV}_{\mathrm{nr}}$ is the sodium nucleus recoil energy threshold of the detector [42]. We thus obtain the event spectrum shown in the left panel of Fig. 1, where the width of the recoil energy bins corresponds to 1 keV$_{\mathrm{ee}}$ [42]. In order to convert an electron recoil energy of 1 keV$_{\mathrm{ee}}$ into the equivalent nuclear recoil energy (i.e., the nuclear recoil

energy giving the same number of photoelectrons as an electron recoil energy of 1 keV), we rely on the recent Na quenching factor measurements of Ref. [43]. Namely, for nuclear recoil energies between 13 and 82 keV$_{\mathrm{nr}}$, we fit the QF data from Fig. 22 of Ref. [43] as a linear function of the nuclear recoil energy. For energies above 82 keV$_{\mathrm{nr}}$ and up to $T_{\max}(\mathrm{Na}) \approx 259$ keV$_{\mathrm{nr}}$, for which no measurements are available, we use a constant quenching factor of 0.23 (estimated from Fig. 4.12 of Ref. [42]), resulting in a constant bin width of 4.33 keV$_{\mathrm{nr}}$. This is larger than the width of the previous bins, thus explaining the little bump at 82 keV$_{\mathrm{nr}}$ in the histogram on the left panel of Fig. 1. On the same plot, we show the expected steady-state background, which we assumed to be flat and equal to its average value of 300 ckkd (counts per keV$_{\mathrm{ee}}$ per kg per day) [42], except in the first two bins where the background is larger. There, we took a conservative value of 400 ckkd. In practice, the number of background events is reduced by a factor of 8000 [42] taking into account the fact that the SNS neutrino beam is pulsed. This reduction factor has been applied in the left panel of Fig. 1.

D. Future cryogenic CsI detector

In addition to the NaI detector, the COHERENT program includes a future cryogenic CsI (Cryo-CsI) detector, with expected improved threshold and detection efficiency with respect to the CsI detector used for the first CEvNS observation. In this paper, we aim to explore the sensitivity of this future Cryo-CsI detector to GNIs and to show how the combination with the future NaI detector can help to break certain degeneracies in the parameter space. For the experimental design, we follow Ref. [44] and assume a

---

[3]As can be seen from Fig. 26 of Ref. [43], the quenching factor for iodine is smaller than 8% over the recoil energy range [0, 80] keV$_{\mathrm{nr}}$. The NaI detector has an electron-equivalent energy threshold of 3 keV$_{\mathrm{ee}}$, which, for QF(I) = 8%, corresponds to a nuclear recoil energy threshold of 37.5 keV$_{\mathrm{nr}}$, not far below the maximal iodine nucleus recoil energy that a neutrino from the SNS beam can induce [$T'_{\max}(\mathrm{I}) \approx 47$ keV$_{\mathrm{nr}}$].

[4]This choice reproduces the energy resolution given in [60] to a good approximation.

10 kg cryogenic CsI detector located at 19.3 m from the neutrino source, like the current CsI detector. Regarding SNS operations, we make the same assumptions as for the NaI detector and consider a total number of protons on target of 1.73×10^{23} per year of data taking. In Ref. [44], it is mentioned that a detector threshold of four photoelectrons (PE) is expected, which we also assume here. To convert this threshold into a nuclear recoil energy, we consider a constant quenching factor of 15% and a light yield of 50 PE/keV$_{ee}$, as indicated in the same reference. Under these assumptions, a 4 PE threshold corresponds to a nuclear recoil energy threshold $T_{th} = 0.533$ keV$_{nr}$. As for the detector efficiency, we consider the same efficiency function as the one provided by the COHERENT Collaboration for the current CsI detector (see the Supplemental Material of Ref. [3]), but with a shift of 8 PE starting at 4 PE in order to account for the fact that a cryogenic detector will improve the efficiency at lower threshold energies. Finally, we neglect smearing between the true recoil energy and the observed number of photoelectrons, as it is estimated to be minimal in Ref. [44], due to the high expected light yield. With these assumptions, we are able to reproduce the expected CEνNS event rate shown in Fig. 3 of Ref. [44]. In the right panel of Fig. 1, we show the expected number of signal events and steady-state background, using the background model of Ref. [44] and applying a reduction factor of 2000, as indicated in Ref. [61]. Note that we adopted the same bin width of 25 PE used in Fig. 2 of Ref. [44] to display their steady-state background model.

IV. ANALYSIS PROCEDURE

For the analysis of the current CsI detector data, we follow the same procedure as Ref. [10] and use the Poissonian χ^2 function,

$$\chi^2(\kappa) = \min_{\xi} \left\{ 2 \sum_{i,j} \left[N_{ij}(\kappa, \xi) - \tilde{N}_{ij} + \tilde{N}_{ij} \ln\left(\frac{\tilde{N}_{ij}}{N_{ij}(\kappa, \xi)}\right) \right] \right.$$
$$\left. + \sum_{m=1}^{2} \frac{\xi_{sig,m}^2}{\sigma_{\xi_{sig,m}}^2} + \sum_{k=1}^{3} \frac{\xi_{bg,k}^2}{\sigma_{\xi_{bg,k}}^2} \right\}, \qquad (17)$$

where i, j run over the nuclear recoil energy and time bins, respectively, $\tilde{N}_{ij}$ is the experimental number of events in bins (i, j), $N_{ij}(\kappa, \xi)$ the predicted number of events in the same bins in the presence of GNIs, κ stands for the set of GNI parameters under test, and ξ is the set of nuisance parameters over which we minimize the expression within braces. $N_{ij}(\kappa, \xi)$ is computed as

$$N_{ij}(\kappa, \xi) = (1 + \xi_{sig,1}) N_{ij}^{sig}(\kappa, \xi_{sig,2}, \xi_1, \xi_2)$$
$$+ (1 + \xi_{bg,1}) N_{ij}^{BRN}(\xi_1) + (1 + \xi_{bg,2}) N_{ij}^{NIN}(\xi_1)$$
$$+ (1 + \xi_{bg,3}) N_{ij}^{SSB}, \qquad (18)$$

where N_{ij}^{sig} is the number of signal events, and N_{ij}^{BRN}, N_{ij}^{NIN}, and N_{ij}^{SSB} are the numbers of beam-related neutron (BRN), neutrino-induced neutron (NIN) and steady-state (SSB) background events, respectively. The signal nuisance parameter $\xi_{sig,1}$ accounts for the detector efficiency, neutrino flux, and quenching factor (QF) normalizations, while $\xi_{sig,2}$ is related to the nuclear radius. The corresponding uncertainties are $\sigma_{\xi_{sig,1}} = 11.45\%$ and $\sigma_{\xi_{sig,2}} = 5\%$ [10]. As for the nuisance parameters $\xi_{bg,k}$, they are associated with the different sources of background: BRN ($\xi_{bg,1}$), NIN ($\xi_{bg,2}$), and SSB ($\xi_{bg,3}$), with corresponding uncertainties $\sigma_{\xi_{bg,1}} = 25\%$, $\sigma_{\xi_{bg,2}} = 35\%$, and $\sigma_{\xi_{bg,3}} = 2.1\%$ [3]. Following Ref. [10], we include in Eq. (17) two additional nuisance parameters ξ_1 and ξ_2, with no penalization term, which account for deviations in the uncertainty on the CEνNS detection efficiency and on beam timing, respectively. By minimizing over all nuisance parameters, we obtain allowed regions at a given confidence level for the GNI parameters under test.

To assess the sensitivity of the future NaI and Cryo-CsI detectors to GNI parameters, we follow Ref. [41] and consider the χ^2 function,

$$\chi^2(\kappa) = \min_{\xi} \left[\sum_i 2 \left\{ N_i(\kappa, \xi) - \tilde{N}_i + \tilde{N}_i \ln\left(\frac{\tilde{N}_i}{N_i(\kappa, \xi)}\right) \right\} \right.$$
$$\left. + \left(\frac{\xi_{sig}}{\sigma_{sig}}\right)^2 + \left(\frac{\xi_{bg}}{\sigma_{bg}}\right)^2 \right], \qquad (19)$$

where we have divided the data in recoil energy bins labeled by i. Since we are dealing with simulated data, we compare the theoretical predictions in the absence and in the presence of GNIs. Hence, we take

$$\tilde{N}_i = N_i^{sig}(SM) + N_i^{bg}, \qquad (20)$$

where $N_i^{sig}(SM)$ represents the number of signal events in bin i predicted by the SM and N_i^{bg} is the simulated steady-state background described in Secs. III C and III D, while

$$N_i(\kappa, \xi) = N_i^{sig}(\kappa)(1 + \xi_{sig}) + N_i^{bg}(1 + \xi_{bg}), \quad (21)$$

where $N_i^{sig}(\kappa)$ is the predicted number of signal events in bin i in the presence of GNIs, and the nuisance parameters ξ_{sig}, ξ_{bg} account for the signal and background normalizations, respectively. For the associated systematic uncertainties, we conservatively assume $\sigma_{sig} = 10\%$ and $\sigma_{bg} = 5\%$ for both detectors. This choice is motivated by the known

values of the uncertainties for the current CsI detector. Notice that, due to the absence of detailed information on the signal and background systematic uncertainties for the NaI and Cryo-CsI detectors, we only consider two nuisance parameters.

Finally, when we perform a combined analysis of future Cryo-CsI and NaI data, we assume the signal and background systematic uncertainties to be fully uncorrelated. In practice, this means that we add the two χ^2 functions for each detector, with independent nuisance parameters ($\xi_{\text{sig}}^{\text{Cryo-CsI}}$, $\xi_{bg}^{\text{Cryo-CsI}}$) and ($\xi_{\text{sig}}^{\text{NaI}}$, ξ_{bg}^{NaI}), respectively. In general, correlations between systematic errors result in stronger constraints on new physics parameters (see, for instance, Ref. [40]). However, the level of correlation between uncertainties in future experiments is difficult to estimate, so we take the conservative approach of assuming fully uncorrelated uncertainties between the two detectors.

V. EXPECTED SENSITIVITIES TO GNI PARAMETERS

In this section, we study the sensitivities to GNI parameters[5] of future NaI and cryogenic CsI detectors with the characteristics described in Sec. III C, and compare their combined expected sensitivities with the constraints set by the current COHERENT CsI detector, which we refer to as CsI (2021). As discussed in Sec. II B, we consider only scalar, vector, and tensor interactions and denote the corresponding couplings by $\varepsilon_{\alpha\beta}^{qS}$, $\varepsilon_{\alpha\beta}^{qV}$ and $\varepsilon_{\alpha\beta}^{qT}$, respectively, with $\alpha, \beta = e, \mu, \tau$ and $q = u, d$.

Since the SNS neutrino beam consists only of electron neutrinos, muon neutrinos, and muon antineutrinos, not all of these parameters can be constrained by CEνNS measurements. Vector GNIs, also known as NSIs, are subject to the Hermiticity condition $\varepsilon_{\beta\alpha}^{qV} = (\varepsilon_{\alpha\beta}^{qV})^*$. As a result, there are six independent parameters for each quark flavor, but only five of them can be constrained at the SNS: two real flavor-diagonal couplings, ε_{ee}^{qV} and $\varepsilon_{\mu\mu}^{qV}$, and three complex flavor off diagonal couplings, $\varepsilon_{e\mu}^{qV}$, $\varepsilon_{e\tau}^{qV}$, and $\varepsilon_{\mu\tau}^{qV}$. In this paper, we study the sensitivities of the NaI and Cryo-CsI detectors to ε_{ee}^{qV}, $\varepsilon_{\mu\mu}^{qV}$, and $\varepsilon_{e\mu}^{qV}$ ($q = u, d$), leaving aside the other off diagonal couplings, which are less constrained.[6]

For scalar and tensor GNIs, the number of independent parameters depends on whether neutrinos are Dirac or Majorana fermions. In this paper, we assume that they are Majorana fermions, both for simplicity and because this

---

[5]From now on, we will use the generic term "GNI parameters" to collectively refer to vector, scalar, and tensor couplings, while vector couplings will also be called "NSI parameters."

[6]This is due to the fact that $\varepsilon_{e\mu}^{qV}$ can induce coherent scatterings for all three components of the SNS neutrino flux, while only ν_e (respectively, ν_μ and $\nu_{\bar{\mu}}$) can scatter off a nucleus via $\varepsilon_{e\tau}^{qV}$ (respectively, $\varepsilon_{\mu\tau}^{qV}$).

possibility is better motivated from a theoretical point of view. Scalar couplings are therefore symmetric, and for each quark flavor, five out of the six independent ones can be constrained by CEνNS measurements at the SNS. However, due to the absence of interference between the scalar and SM contributions to the CEνNS cross section, the same constraints apply to ε_{ee}^{qS} and $\varepsilon_{e\tau}^{qS}$, as well as to $\varepsilon_{\mu\mu}^{qS}$ and $\varepsilon_{\mu\tau}^{qS}$. It is therefore sufficient to study the sensitivities of the CsI and NaI detectors to the scalar couplings ε_{ee}^{qS}, $\varepsilon_{\mu\mu}^{qS}$, and $\varepsilon_{e\mu}^{qS}$ ($q = u, d$). Finally, tensor couplings are antisymmetric for Majorana neutrinos, leaving only three independent parameters $\varepsilon_{e\mu}^{qT}$, $\varepsilon_{e\tau}^{qT}$, and $\varepsilon_{\mu\tau}^{qT}$ for each value of q, all of which can induce scatterings of SNS neutrinos off nuclei.

Throughout this paper, we assume all GNI couplings to be real. The upper bounds on these parameters obtained from the currently available CsI data and the expected sensitivity of the future NaI and Cryo-CsI detectors are determined following the numerical procedure described in Sec. IV.

A. Expected sensitivities to individual GNI parameters

We first consider the expected sensitivities of the future NaI and Cryo-CsI detectors to individual parameters; i.e., we consider a single nonvanishing coupling at a time. Note that in this case, the assumption of real couplings does not mean any loss of generality, as the CEνNS cross section only depends on the moduli of the GNI parameters (except for flavor-diagonal vector couplings, which are real and can interfere with the SM contribution).

Figure 2 shows the expected sensitivities of the future detectors to the flavor-diagonal vector couplings ε_{ee}^{uV} (left panel) and $\varepsilon_{\mu\mu}^{uV}$ (right panel) after 3 years of data taking at the SNS, assuming conservatively, $\sigma_{\text{sig}} = 10\%$ and $\sigma_{bg} = 5\%$. In both panels, the blue dotted curves correspond to the NaI detector, and the green dash-dotted curves to the Cryo-CsI detector. Two degenerate minima can be observed in the $\Delta\chi^2$ profiles, as a result of the interference between the SM and NSI contributions to the CEνNS cross section. Indeed, Eq. (6) contains a term proportional to (where we have set $\varepsilon_{\alpha\alpha}^{dV} = 0$ and neglected a term suppressed by $g_V^p \ll 1$)

$$|C_{\alpha\alpha}^V + Q_{W,\alpha}|^2 \simeq N^2 \left|\left(2\frac{Z}{N} + 1\right)\varepsilon_{\alpha\alpha}^{uV} - \frac{1}{2}\right|^2, \quad (22)$$

implying the existence of a second $\Delta\chi^2$ minimum at $\varepsilon_{\alpha\alpha}^{uV} \simeq 1/(2Z/N + 1)$, i.e., $\simeq 0.34$ for NaI and $\simeq 0.40$ for CsI (taking into account the fact that the NaI detector is only sensitive to Na recoils, and that Cs and I have approximately the same Z/N). The sharp rise of the $\Delta\chi^2$ functions between the two minima is due to the fact that for
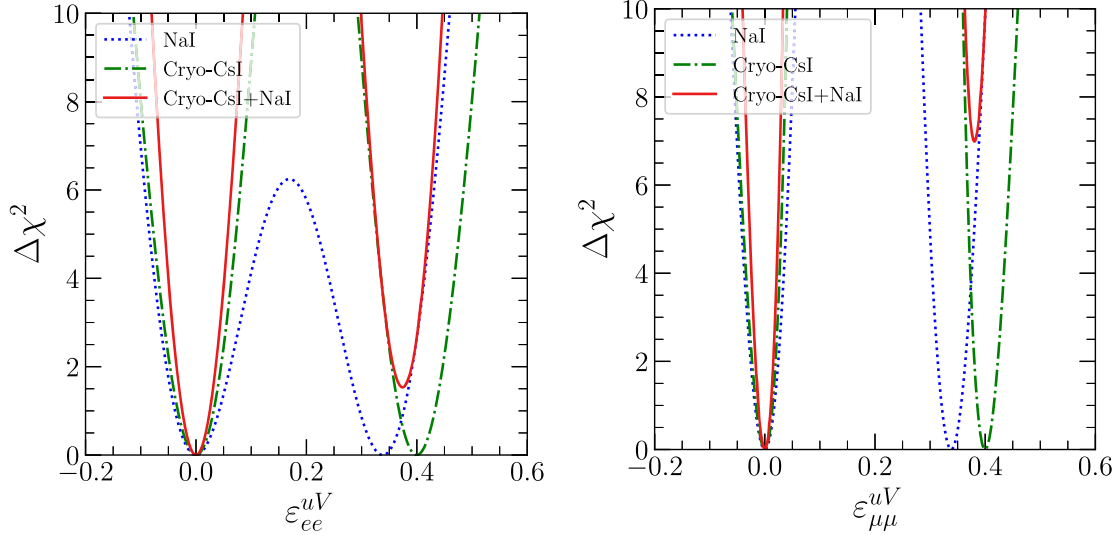
FIG. 2. Expected one-dimensional $\Delta\chi^2$ profiles for the vector couplings ε_{ee}^{uV} (left panel) and $\varepsilon_{\mu\mu}^{uV}$ (right panel). The blue dotted curves (respectively, the green dash-dotted curves) represent the expected sensitivities of the NaI detector described in Sec. III C (respectively, the Cryo-CsI detector described in Sec. III D), assuming 3 years of data taking at the SNS. The solid red curves correspond to the combined NaI + Cryo-CsI analysis.

$\varepsilon_{\alpha\alpha}^{uV} \simeq 1/2(2Z/N + 1)$, the NSI and SM contributions to $\nu_\alpha/\bar{\nu}_\alpha$ scatterings completely cancel out, resulting in a reduction of the predicted number of CEνNS events by roughly 2/3 for $\alpha = \mu$ and 1/3 for $\alpha = e$, in strong tension with data.

Figure 2 also shows the expected sensitivity to ε_{ee}^{uV} and $\varepsilon_{\mu\mu}^{uV}$ from a combined analysis of the data of the future NaI and Cryo-CsI detectors (solid red curve), assuming 3 years of data taking for each detector. The advantage of such a combination is to lift the degeneracy between the two minima of the $\Delta\chi^2$ function: since the location of the second minimum is different for NaI and Cryo-CsI (as a consequence of the different proton-to-neutron ratios of their material targets), it is difficult to fit SM-like experimental data in both detectors with a nonzero value of $\varepsilon_{\alpha\alpha}^{uV}$. In particular, the second $\Delta\chi^2$ minimum is disfavored at more than 99% CL for $\varepsilon_{\mu\mu}^{uV}$ (but only at a bit more than 1σ for ε_{ee}^{uV}, due to the smaller number of ν_e-induced CEνNS events).

Having demonstrated the interest of performing a combined analysis of the data from the future NaI and Cryo-CsI detectors, we study in the following the expected sensitivities to GNI parameters of this detector combination, and we compare them with the constraints obtained from the currently available CsI data. The results for vector couplings are shown in Fig. 3, where the $\Delta\chi^2$ functions defined in Sec. IV are plotted against the parameter assumed to be nonvanishing (from left to right: ε_{ee}^{qV}, $\varepsilon_{e\mu}^{qV}$, and $\varepsilon_{\mu\mu}^{qV}$, with $q = u$ in the upper panels and $q = d$ in the lower panels). The black dashed curves show the constraints obtained from the currently available

(2021) COHERENT CsI data[7] and are consistent with the results obtained in Ref. [10]. The solid red curves represent the expected sensitivities of the combination of the future NaI and Cryo-CsI detectors after 3 years of data taking, assuming again $\sigma_{\text{sig}} = 10\%$ and $\sigma_{\text{bg}} = 5\%$. Table II summarizes the 90% CL and 2σ expected sensitivities to vector couplings of the NaI + Cryo-CsI detector combination, as well as the constraints on the same parameters from the COHERENT CsI 2021 data.

As can be seen from Fig. 3 and Table II, a clear improvement of the constraints on flavor-diagonal vector couplings is expected from the combination of the future NaI and Cryo-CsI detectors, already with 3 years of data taking. This is partly due to the larger statistics of these detectors. However, the most noticeable feature, namely the fact that the second minimum of the $\Delta\chi^2$ function tends to be disfavored (most notably for the parameter $\varepsilon_{\mu\mu}^{uV}$, and to a lesser extent for ε_{ee}^{uV} and $\varepsilon_{\mu\mu}^{dV}$), cannot be explained by statistics alone, but it is a consequence of the different proton-to-neutron ratios of the Na and CsI targets, as explained before. A similar result can be obtained by suitably choosing combinations of the detectors proposed for CEνNS measurements at the European Spallation Source [26], such as CsI + Si and Xe + Si, as shown in Ref. [41].

---

[7]Note that for the CsI detector, the first minimum of the $\Delta\chi^2$ function for flavor-diagonal NSI parameters is not located at $\varepsilon_{\alpha\alpha}^{qV} = 0$ ($\alpha = e, \mu$; $q = u, d$). This is due to the fact that we are analysing real data, which does not exactly match the SM prediction.
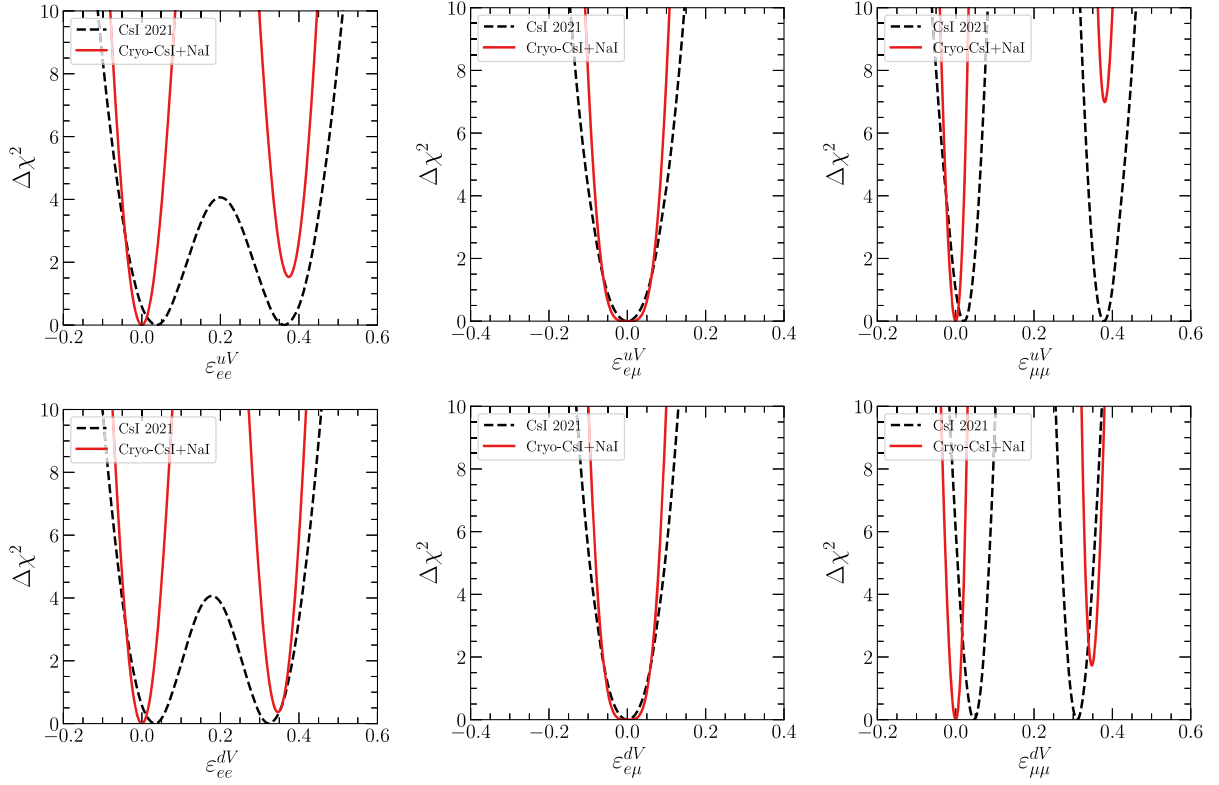
FIG. 3. One-dimensional $\Delta\chi^2$ profiles for the vector coupling ε_{ee}^{qV} (left panels), $\varepsilon_{e\mu}^{qV}$ (middle panels), and $\varepsilon_{\mu\mu}^{qV}$ (right panels), with $q = u$ in the upper panels and $q = d$ in the lower panels. The black dashed curves are obtained using the currently available data of the COHERENT CsI detector. The solid red curves represent the expected sensitivities of the combination of the future NaI and Cryo-CsI detectors, assuming 3 years of data taking at the SNS for each detector. The flavor off diagonal NSI parameter $\varepsilon_{e\mu}^{qV}$ is assumed to be real.

For flavor off diagonal vector couplings (middle panels) of Fig. 3), only a small improvement on the current constraints (mainly visible at $\gtrsim 3\sigma$ confidence level) is expected from the combination of the future NaI and Cryo-CsI detectors, in spite of a larger statistics. The main reason for this is that the COHERENT CsI detector measured less

events than predicted by the SM, while off diagonal vector couplings can only increase the CEνNS cross section, due to the absence of an interference term with the SM contribution. As a result, the CsI (2021) constraints on these parameters are better than expected. By contrast, flavor-diagonal vector couplings interfere with the SM

TABLE II. Sensitivities to the vector couplings ε_{ee}^{qV}, $\varepsilon_{e\mu}^{qV}$, and $\varepsilon_{\mu\mu}^{qV}$ ($q = u, d$) at the 90% and 2σ confidence levels with 1 degree of freedom (i.e., $\Delta\chi^2 \leq 2.71$ and $\Delta\chi^2 \leq 4$, respectively). For the CsI detector, the intervals actually correspond to the ranges of parameter values allowed by the currently available data, while for the combination of the future NaI and Cryo-CsI detectors, they represent the expected sensitivities assuming 3 years of data taking at the SNS for each detector. The flavor off diagonal NSI parameter $\varepsilon_{e\mu}^{qV}$ is assumed to be real.

| Detector	q	ε_{ee}^{qV}		$\varepsilon_{e\mu}^{qV}$		$\varepsilon_{\mu\mu}^{qV}$	
		90% CL	2σ CL	90% CL	2σ CL	90% CL	2σ CL
CsI (2021)	u	$[-0.04, 0.134]$ $\cup [0.266, 0.440]$	$[-0.056, 0.186]$ $\cup [0.212, 0.456]$	$[-0.081, 0.081]$	$[-0.097, 0.097]$	$[-0.015, 0.053]$ $\cup [0.346, 0.414]$	$[-0.024, 0.060]$ $\cup [0.34, 0.424]$
	d	$[-0.035, 0.120]$ $\cup [0.237, 0.393]$	$[-0.05, 0.168]$ $\cup [0.190, 0.408]$	$[-0.073, 0.073]$	$[-0.087, 0.087]$	$[-0.016, 0.075]$ $\cup [0.282, 0.340]$	$[-0.010, 0.081]$ $\cup [0.276, 0.347]$
NaI + Cryo-CsI	u	$[-0.041, 0.042]$ $\cup [0.347, 0.4]$	$[-0.05, 0.051]$ $\cup [0.335, 0.412]$	$[-0.073, 0.073]$	$[-0.082, 0.082]$	$[-0.019, 0.018]$	$[-0.024, 0.021]$
	d	$[-0.037, 0.038]$ $\cup [0.311, 0.385]$	$[-0.046, 0.047]$ $\cup [0.302, 0.389]$	$[-0.067, 0.067]$	$[-0.075, 0.075]$	$[-0.018, 0.016]$ $\cup [0.338, 0.358]$	$[-0.022, 0.020]$ $\cup [0.333, 0.363]$
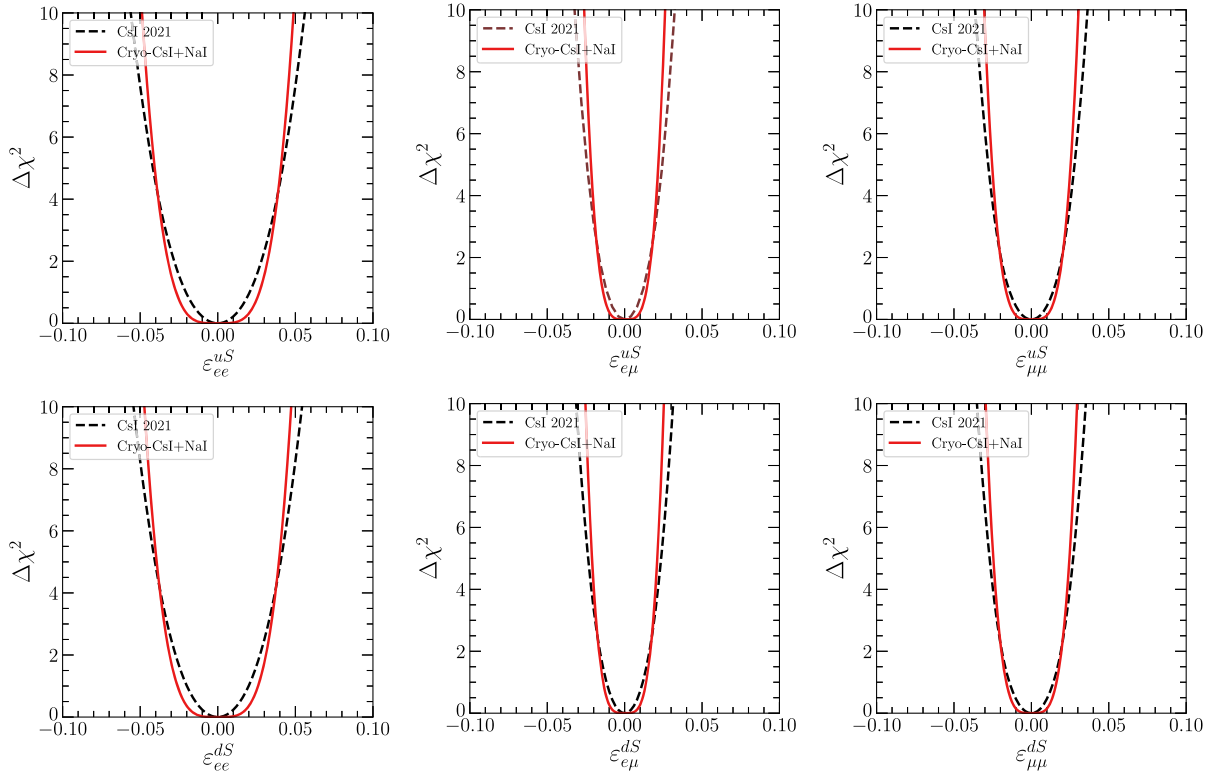
FIG. 4. Same as Fig. 3, but for the scalar couplings ε_{ee}^{qS} (left panels), $\varepsilon_{e\mu}^{qS}$ (middle panels), and $\varepsilon_{\mu\mu}^{qS}$ (right panels), with $q = u$ in the upper panels and $q = d$ in the lower panels. All couplings are assumed to be real.

contribution and can therefore fit a deficit of observed CEνNS events. This is the reason why, in Fig. 3, the first minimum of the black dashed curves for flavor-diagonal vector couplings is shifted from zero.

Let us now move on to the results for scalar GNIs. As explained before, CEνNS measurements at the SNS only give six independent constraints on scalar couplings, since $\varepsilon_{e\tau}^{qS}$ and $\varepsilon_{\mu\tau}^{qS}$ contribute the same way to the CEνNS cross section as ε_{ee}^{qS} and $\varepsilon_{\mu\mu}^{qS}$, respectively.[8] We therefore only present results for the six scalar couplings ε_{ee}^{qS}, $\varepsilon_{\mu\mu}^{qS}$, and $\varepsilon_{e\mu}^{qS}$ ($q = u$, d). The $\Delta\chi^2$ profiles are displayed in Fig. 4, with the same color code as before, and the 90% CL and 2σ expected sensitivities of the NaI + Cryo-CsI detector combination, together with the constraints from the COHERENT CsI 2021 data, are given in Table III. As can be seen by comparing Figs. 3 and 4, the results for scalar couplings are similar to the ones for off diagonal vector couplings, which is not a surprise since both types of interactions share the property of not interfering with the SM contribution in the CEνNS cross section. In particular, we only expect a small improvement of the constraints on

scalar couplings from the NaI + Cryo-CsI detector combination, mainly visible at the $\gtrsim 3\sigma$ confidence level.

Finally, the results for tensor GNIs are shown in Fig. 5 and Table IV. Recall that there are only six independent tensor couplings if, as assumed in this paper, neutrinos are Majorana fermions, namely, $\varepsilon_{e\mu}^{qT}$, $\varepsilon_{e\tau}^{qT}$, and $\varepsilon_{\mu\tau}^{qT}$ ($q = u$, d). Comparing the expected sensitivities of the NaI + Cryo-CsI detector combination with the constraints from the COHERENT CsI 2021 data (see Table IV), we only expect a small improvement of the constraints on tensor couplings involving an up quark.

B. Expected sensitivities to pairs of GNI parameters

In this section, we study the expected sensitivity of the future NaI and Cryo-CsI detectors to pairs of GNI parameters; i.e., we consider two nonvanishing couplings at a time. As is well known, this situation leads to degeneracies in the form of extended allowed regions in the two-dimensional GNI parameter space. Combining data on target nuclei characterized by different proton to neutron ratios can help to reduce these degeneracies, as shown, e.g., in Refs. [8,26,41]. In the case of the future NaI and cryogenic CsI detectors studied in this paper, the target materials significantly differ by their proton to neutron ratios: 0.92 for sodium (the NaI detector is not sensitive to

---

[8]This statement holds for symmetric scalar couplings, hence, for Majorana neutrinos (as assumed in this paper), but not for Dirac neutrinos.

TABLE III. Same as Table II, but for the scalar couplings ε_{ee}^{qS}, $\varepsilon_{e\mu}^{qS}$, and $\varepsilon_{\mu\mu}^{qS}$ ($q = u, d$).

Detector	q	ε_{ee}^{qS} 90% CL	2σCL	$\varepsilon_{e\mu}^{qS}$ 90% CL	2σCL	$\varepsilon_{\mu\mu}^{qS}$ 90% CL	2σCL
CsI (2021)	u	[−0.032, 0.032]	[−0.038, 0.038]	[−0.018, 0.018]	[−0.022, 0.022]	[−0.022, 0.022]	[−0.026, 0.026]
	d	[−0.031, 0.031]	[−0.037, 0.037]	[−0.018, 0.018]	[−0.022, 0.022]	[−0.022, 0.022]	[−0.025, 0.025]
NaI + Cryo-CsI	u	[−0.034, 0.034]	[−0.038, 0.038]	[−0.018, 0.018]	[−0.02, 0.02]	[−0.021, 0.021]	[−0.023, 0.023]
	d	[−0.033, 0.033]	[−0.037, 0.037]	[−0.017, 0.017]	[−0.019, 0.019]	[−0.021, 0.021]	[−0.023, 0.023]

iodine recoils) versus 0.71 and 0.72 for cesium and iodine, both of which contribute to the CEνNS rate in the Cryo-CsI detector.

We begin our analysis by studying the case where the two nonvanishing GNI parameters are of vector type (i.e., NSIs). Many different pairs of NSI parameters can be considered; we only present results for a few representative examples, as the other possible choices are characterized by similar allowed regions. As we did in the previous subsection, we start our discussion by presenting in Fig. 6 the expected individual sensitivities of the future NaI and Cryo-CsI detectors to two different pairs of (flavor-diagonal) NSI parameters: $(\varepsilon_{ee}^{uV}, \varepsilon_{\mu\mu}^{uV})$ in the left panel, and $(\varepsilon_{\mu\mu}^{uV}, \varepsilon_{\mu\mu}^{dV})$ in the right panel. The expected 90% CL allowed regions are enclosed by blue dotted lines for NaI and by green dash-dotted contours for Cryo-CsI, assuming as in the previous Sec. III years of data taking and $\sigma_{\rm sig} = 10\%$, $\sigma_{\rm bg} = 5\%$.

The ellipticlike shape of the allowed regions for the NSI parameters $(\varepsilon_{ee}^{uV}, \varepsilon_{\mu\mu}^{uV})$ (left panel of Fig. 6) can be understood from the expression for the predicted CEνNS rate in each reconstructed nuclear recoil energy bin [41]. For a single-nucleus detector,[9] the predicted number of events in the recoil energy bin $[T_i, T_{i+1}]$ can be written as

$$N_i^{th} = C_i^e (2Z + N)^2 \left(\varepsilon_{ee}^{uV} + \frac{Z g_V^p + N g_V^n}{2Z + N} \right)^2$$
$$+ C_i^\mu (2Z + N)^2 \left(\varepsilon_{\mu\mu}^{uV} + \frac{Z g_V^p + N g_V^n}{2Z + N} \right)^2, \quad (23)$$

where C_i^e (respectively, C_i^μ) is the number obtained by performing the integral over E_{ν_e} (respectively, E_{ν_μ} and $E_{\bar\nu_\mu}$) and the true and reconstructed nuclear recoil energies in Eq. (15), after having factorized out $|C_{\alpha\alpha}^V + Q_{W,\alpha}|^2$. Equation (23) is the equation of an ellipse with semi-major and semiminor axes [given, respectively, by $\sqrt{N_i^{th}/C_i^e (2Z + N)^2}$ and $\sqrt{N_i^{th}/C_i^\mu (2Z + N)^2}$] that depend on both the nucleus and the energy bin (the center of the ellipse also depends on the nucleus). All sets of

---

[9]The NaI detector is only sensitive to Na recoils, so can be considered single-nucleus. As for the Cryo-CsI detector, its two target nuclei have approximately the same numbers of protons and neutrons.

$(\varepsilon_{ee}^{uV}, \varepsilon_{\mu\mu}^{uV})$ values lying on this ellipse predict the same number of CEνNS events in the ith energy bin, but not necessarily in the other bins, resulting in an approximate degeneracy between these two parameters. This explains why the expected 90% CL region allowed by the Cryo-CsI detector has the form of an approximate, partly broken ellipse (for the NaI detector, the allowed region turns out to be an almost perfect ellipse). Note that the NaI and Cryo-CsI allowed areas do not fully overlap, as both the center and the semi-axes of the ellipses depend on the nucleus. If we now consider the 90% CL region allowed by the combination of the future NaI and Cryo-CsI detectors, shown in red in the left panel of Fig. 6, we can see that the degeneracy between the vector couplings ε_{ee}^{uV} and $\varepsilon_{\mu\mu}^{uV}$ is partially broken. Namely, the allowed region reduces to a crescent, approximately corresponding to the intersection of the NaI and Cryo-CsI ellipses. This result illustrates the benefit of combining data from detectors with different proton-to-neutron ratios in order to reduce degeneracies between flavor-diagonal NSI parameters.

Let us now consider the right panel of Fig. 6, which displays the 90% CL allowed regions for the flavor-diagonal NSI parameters $(\varepsilon_{\mu\mu}^{uV}, \varepsilon_{\mu\mu}^{dV})$. In this case, the individual NaI and Cryo-CsI allowed regions consist of two parallel bands [9]. This is a consequence of the fact that, for a single-nucleus target (or a target composed of two nuclei with approximately the same proton to neutron ratio, like CsI), the CEνNS cross section depends on the flavor-diagonal NSI parameters $\varepsilon_{\alpha\alpha}^{uV}$ and $\varepsilon_{\alpha\alpha}^{dV}$ only through the modulus of the combination,

$$C_{\alpha\alpha}^V + Q_{W,\alpha} \simeq (Z + 2N)(\varepsilon_{\alpha\alpha}^{dV} - m\varepsilon_{\alpha\alpha}^{uV}) - \frac{1}{2}, \quad m = -\frac{2Z + N}{Z + 2N}, \quad (24)$$

in which we neglected a term suppressed by $g_V^p \ll 1$. Thus, values of $\varepsilon_{\alpha\alpha}^{uV}$ and $\varepsilon_{\alpha\alpha}^{dV}$ lying on a straight line with slope m [8] produce the same number of CEνNS events in each recoil energy bin. This is an example of the degeneracies mentioned above. It follows that the parameter space region allowed by SM-like experimental data at a given confidence interval (here, 90% CL) consists of two parallel bands around the straight lines $\varepsilon_{\alpha\alpha}^{dV} - m\varepsilon_{\alpha\alpha}^{uV} = 0$ and
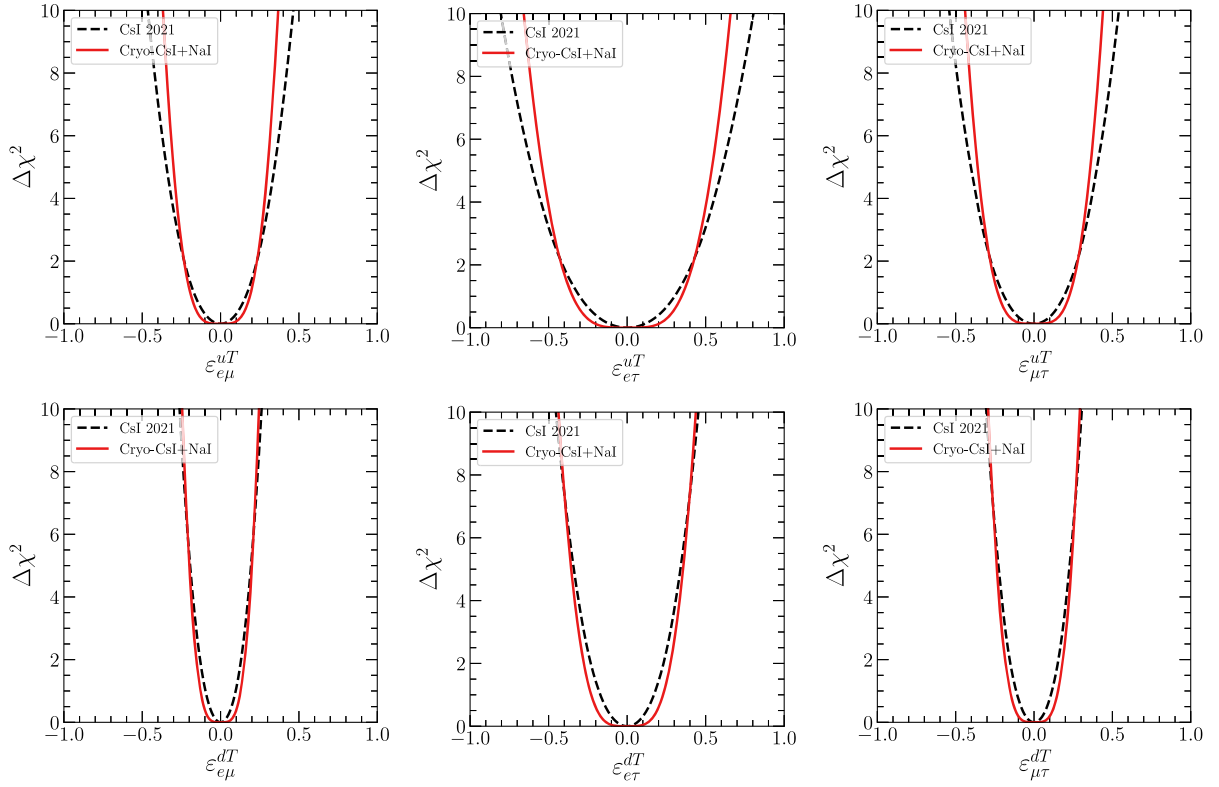
FIG. 5. Same as Fig. 3, but for the tensor couplings $\varepsilon_{e\mu}^{qT}$ (left panels), $\varepsilon_{e\tau}^{qT}$ (middle panels), and $\varepsilon_{\mu\tau}^{qT}$ (right panels), with $q = u$ in the upper panels and $q = d$ in the lower panels. All couplings are assumed to be real.

$\varepsilon_{\alpha\alpha}^{dV} - m\varepsilon_{\alpha\alpha}^{uV} = 1/(Z + 2N)$. This is indeed what we can observe in the right panel of Fig. 6 for the individual NaI and Cryo-CsI allowed regions. Note that the slopes of the bands differ due to the different proton-to-neutron ratios of the two detectors. Thus, combining the results of the two detectors leads to a partial breaking of the degeneracies between the flavor-diagonal NSI parameters $\varepsilon_{\mu\mu}^{uV}$ and $\varepsilon_{\mu\mu}^{dV}$, as can be seen in the right panel of Fig. 6, where the two infinite bands reduce to the red closed areas.

Now that we have shown the impact of a combined NaI + Cryo-CsI analysis on degeneracies between flavor-diagonal NSI parameters, we are ready to compare the expected sensitivities of this combined analysis with the constraints obtained from the COHERENT CsI 2021 data.

Figure 7 displays the allowed regions at the 90% confidence level for four different pairs of vector couplings. The upper panels correspond to combinations of flavor-diagonal couplings involving the same lepton flavor but different quarks, namely $(\varepsilon_{ee}^{uV}, \varepsilon_{ee}^{dV})$ in the left panel and $(\varepsilon_{\mu\mu}^{uV}, \varepsilon_{\mu\mu}^{dV})$ in the right panel. By contrast, the lower panels correspond to pairs of vector couplings involving the same quark but different lepton flavors. The combination in the left panel, $(\varepsilon_{ee}^{uV}, \varepsilon_{\mu\mu}^{uV})$, involves two flavor-diagonal couplings, while the one in the right panel, $(\varepsilon_{e\mu}^{uV}, \varepsilon_{\mu\mu}^{uV})$, involves a flavor-diagonal and an off diagonal coupling. In all cases, the regions enclosed by black dashed lines are the ones allowed at the 90% confidence level by the current CsI data (these allowed regions were first presented in Ref. [10], and are

TABLE IV. Same as Table II, but for the tensor couplings $\varepsilon_{e\mu}^{qT}$, $\varepsilon_{e\tau}^{qT}$, and $\varepsilon_{\mu\tau}^{qT}$ ($q = u, d$).

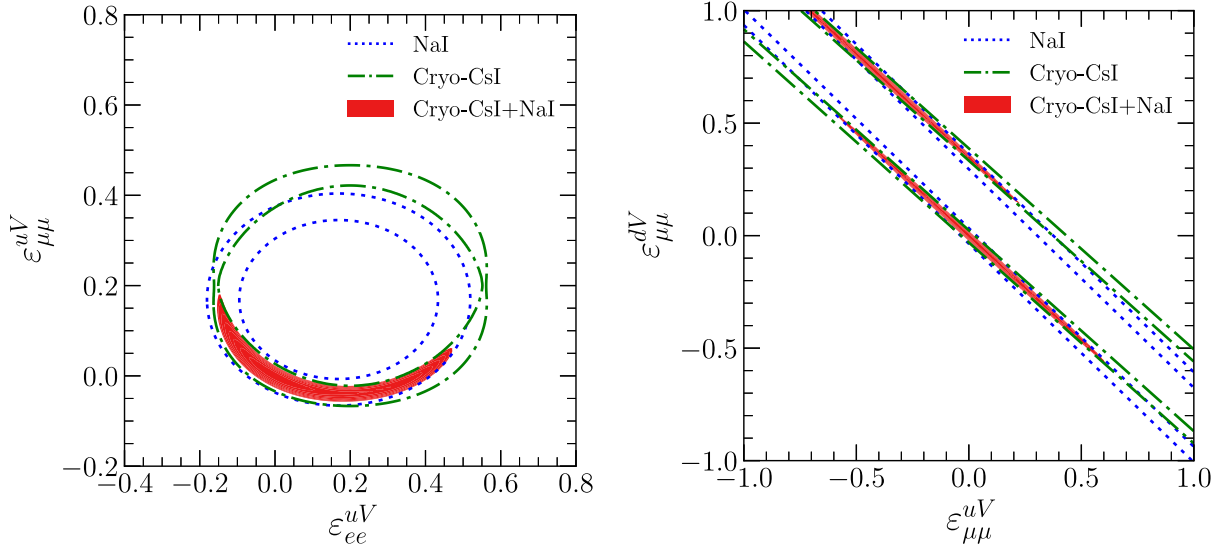| Detector | q | $\varepsilon_{e\mu}^{qT}$ | | $\varepsilon_{e\tau}^{qT}$ | | $\varepsilon_{\mu\tau}^{qT}$ | |
		90% CL	2σCL	90% CL	2σCL	90% CL	2σCL
CsI (2021)	u	$[-0.265, 0.265]$	$[-0.314, 0.314]$	$[-0.467, 0.467]$	$[-0.55, 0.55]$	$[-0.314, 0.314]$	$[-0.369, 0.369]$
	d	$[-0.15, 0.15]$	$[-0.177, 0.177]$	$[-0.264, 0.264]$	$[-0.310, 0.310]$	$[-0.177, 0.177]$	$[-0.208, 0.208]$
NaI + Cryo-CsI	u	$[-0.253, 0.253]$	$[-0.282, 0.282]$	$[-0.453, 0.453]$	$[-0.505, 0.505]$	$[-0.303, 0.303]$	$[-0.337, 0.337]$
	d	$[-0.167, 0.167]$	$[-0.187, 0.187]$	$[-0.299, 0.299]$	$[-0.334, 0.334]$	$[-0.200, 0.200]$	$[-0.223, 0.223]$

FIG. 6.   Expected 90% CL allowed regions (with 2 degrees of freedom, i.e. $\Delta\chi^2 \leq 4.61$) for the pairs of NSI parameters $(\varepsilon_{ee}^{uV}, \varepsilon_{\mu\mu}^{uV})$ (left panel) and $(\varepsilon_{\mu\mu}^{uV}, \varepsilon_{\mu\mu}^{dV})$ (right panel). The blue dotted contours (respectively, the green dash-dotted contours) correspond to the expected constraints from the NaI detector described in Sec. III C (respectively, the Cryo-CsI detector described in Sec. III D), assuming 3 years of data taking at the SNS. The red regions represent the expected combined sensitivities of the two detectors.

shown here for reference), while the red areas correspond to the expected sensitivity of the NaI + Cryo-CsI combination, assuming 3 years of data taking at the SNS for each detector. For all pairs of NSI parameters considered here, the expected future sensitivities represent a clear improvement on the current CsI constraints. This is due to two main factors: the increase in statistics, and the different proton-to-neutron ratios of the NaI and CsI targets, whose impact on parameter degeneracies has been discussed above.

In the upper panels, in addition to the degeneracy breaking, the effect of the larger statistics is clearly visible, especially in the $(\varepsilon_{ee}^{uV}, \varepsilon_{ee}^{dV})$ parameter space. While the two bands associated with the current CsI detector overlap, due to the limited statistics in the ν_e channel (there are twice as many ν_μ's and $\bar{\nu}_\mu$'s as ν_e's in the SNS neutrino beam), the expected allowed region for the NaI + Cryo-CsI combination consists of two disconnected areas. For the pairs of NSI parameters $(\varepsilon_{ee}^{uV}, \varepsilon_{\mu\mu}^{uV})$ (lower left panel), the region allowed by the current CsI detector is a broken ellipse, with no points around $\varepsilon_{\mu\mu}^{uV} \simeq 1/2(2Z/N + 1) \approx 0.2$, where the NSI and SM contributions to ν_μ- and $\bar{\nu}_\mu$-induced CEνNS completely cancel out. This leaves two degenerate allowed regions around $\varepsilon_{\mu\mu}^{uV} = 0$ and $\varepsilon_{\mu\mu}^{uV} \simeq 1/(2Z/N + 1) \approx 0.4$, while only the red area is expected to survive the degeneracy breaking enforced by the NaI + Cryo-CsI combination [see the discussion around Eq. (23)].

Finally, we also observe an ellipse-shaped degeneracy between the vector couplings $\varepsilon_{e\mu}^{uV}$ and $\varepsilon_{\mu\mu}^{uV}$ in the lower

right panel of Fig. 7, which is not broken by the current CsI data. This can be understood by noting that $\varepsilon_{e\mu}^{uV}$ induces both ν_e and $\nu_\mu/\bar{\nu}_\mu$ coherent scatterings on the target nuclei, without interfering with the SM contribution. Nonvanishing values of $\varepsilon_{e\mu}^{uV}$ can therefore compensate for the destructive interference between the SM and $\varepsilon_{\mu\mu}^{uV}$ contributions to the CEνNS cross section, which would otherwise reduce the number of $\nu_\mu/\bar{\nu}_\mu$-induced signal events. As a result, the ellipse is not broken around $\varepsilon_{\mu\mu}^{uV} \approx 0.2$ in the case of the current CsI detector. This degeneracy is, however, expected to be broken by the NaI + Cryo-CsI combination, for the same reason as for the $(\varepsilon_{ee}^{uV}, \varepsilon_{\mu\mu}^{uV})$ pair: due to the different proton-to-neutron ratios of the NaI and CsI targets, the corresponding ellipses do not fully overlap, leaving only the allowed red region in the lower right panel of Fig. 7.

Let us now consider scalar and tensor GNIs. Figure 8 shows the 90% CL allowed regions for two different pairs of scalar couplings with the same lepton flavor indices: $(\varepsilon_{e\mu}^{uS}, \varepsilon_{e\mu}^{dS})$ in the left panel, and $(\varepsilon_{\mu\mu}^{uS}, \varepsilon_{\mu\mu}^{dS})$ in the right panel. As in Fig. 7, the regions allowed by the current CsI data are within black dashed lines, while the red areas correspond to the expected sensitivity of the NaI + Cryo-CsI combination, assuming 3 years of data taking at the SNS for each detector. Since the scalar couplings $\varepsilon_{\alpha\beta}^{uS}$ and $\varepsilon_{\alpha\beta}^{dS}$ contribute to the CEνNS cross section through the linear combination $C_{\alpha\beta}^S$, given in Eq. (7), the allowed regions are straight bands around a line passing through the origin (as a consequence of the fact that scalar
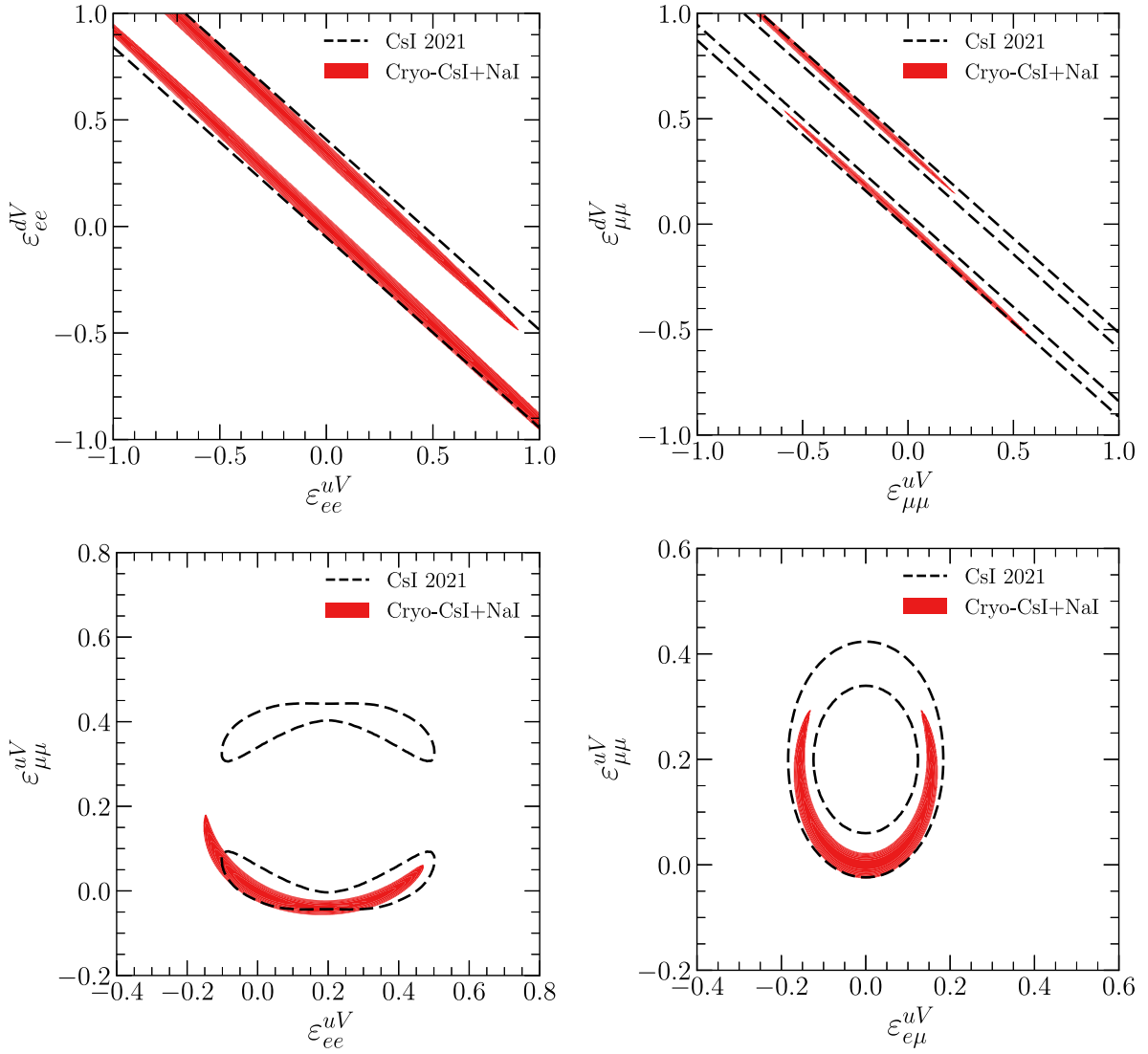
FIG. 7. 90% CL allowed regions (with 2 degrees of freedom, i.e., $\Delta\chi^2 \leq 4.61$) for different pairs of NSI parameters: $(\varepsilon_{ee}^{uV}, \varepsilon_{ee}^{dV})$ (upper left panel), $(\varepsilon_{\mu\mu}^{uV}, \varepsilon_{\mu\mu}^{dV})$ (upper right panel), $(\varepsilon_{ee}^{uV}, \varepsilon_{\mu\mu}^{uV})$ (lower left panel), and $(\varepsilon_{e\mu}^{uV}, \varepsilon_{\mu\mu}^{uV})$ (lower right panel). The regions enclosed by black dashed lines correspond to the constraints from the currently available CsI data, while the red areas represent the expected sensitivities of the combined NaI + Cryo-CsI analysis with the detector characteristics described in Sec. III, assuming 3 years of data taking at the SNS for each detector. The flavor off diagonal parameter $\varepsilon_{e\mu}^{qV}$ is assumed to be real.

couplings do not interfere with the SM contribution). While the slope of this line depends on the proton to neutron ratio of the target nucleus, it is in practice very close to -1 for Cs, I and Na. A consequence of this is that even though sodium has a different proton to neutron ratio than cesium and iodine, the NaI + Cryo-CsI combination is unable to reduce the degeneracy between $\varepsilon_{\alpha\beta}^{uS}$ and $\varepsilon_{\alpha\beta}^{dS}$.

Finally, Fig. 9 displays the 90% CL allowed regions for the pairs of tensor couplings $(\varepsilon_{e\mu}^{uT}, \varepsilon_{e\mu}^{dT})$ (left panel)

and $(\varepsilon_{\mu\tau}^{uT}, \varepsilon_{\mu\tau}^{dT})$ (right panel). Qualitatively, similar features to the scalar case can be observed, except that CEνNS is much less sensitive to tensor couplings, and that the line slope has a different dependence on the proton to neutron ratio of the target nucleus. This explains the shape of the expected allowed NaI + Cryo-CsI region, but the poor sensitivity of CEνNS to tensor GNI parameters makes it difficult to reduce the degeneracy between $\varepsilon_{\alpha\beta}^{uT}$ and $\varepsilon_{\alpha\beta}^{dT}$ more significantly than can be seen in Fig. 9.
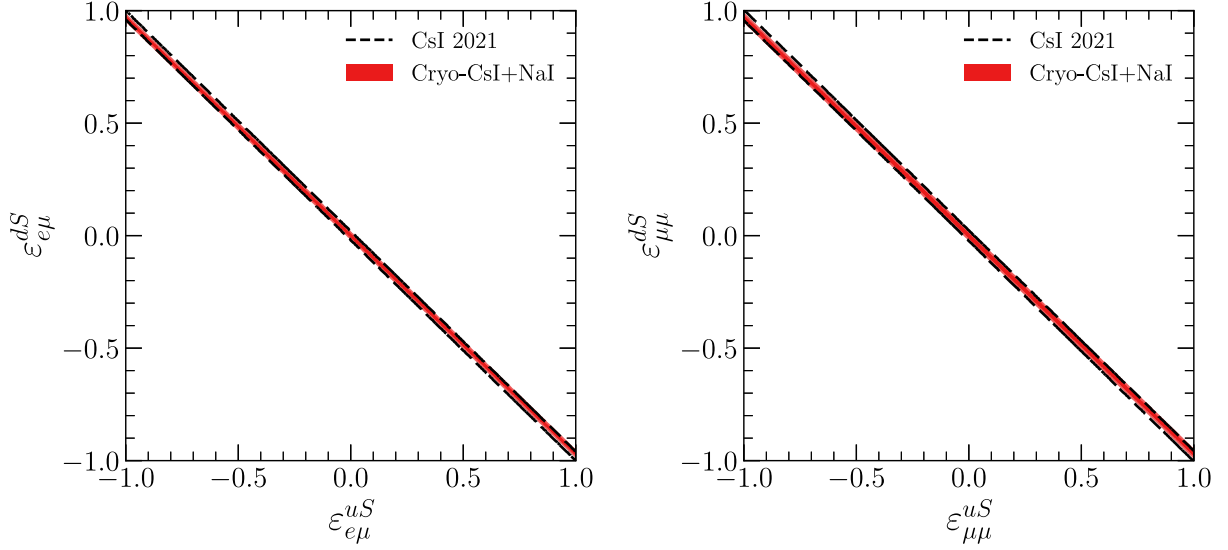
FIG. 8. 90% CL allowed regions for the pairs of scalar GNI parameters $(\varepsilon_{e\mu}^{uS}, \varepsilon_{e\mu}^{dS})$ (left panel) and $(\varepsilon_{\mu\mu}^{uS}, \varepsilon_{\mu\mu}^{dS})$ (right panel). The regions enclosed by black dashed lines correspond to the constraints from the currently available CsI data, while the red areas represent the expected sensitivities of the combined NaI + Cryo-CsI analysis with the detector characteristics described in Sec. III, assuming 3 years of data taking at the SNS for each detector. All GNI parameters are assumed to be real.
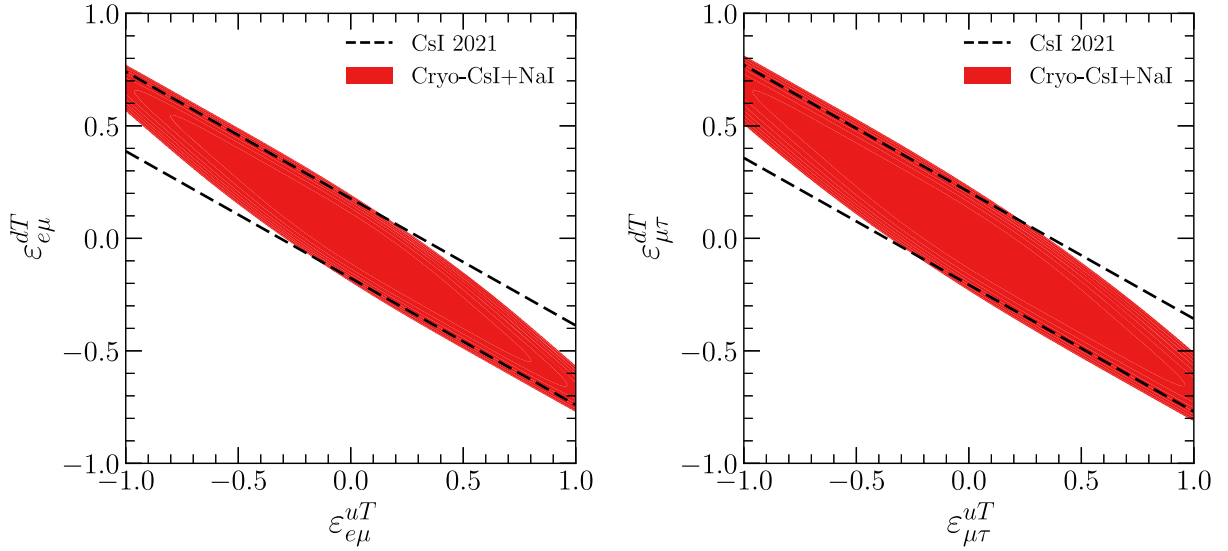
FIG. 9. Same as Fig. 8, but for the pairs of tensor GNI parameters $(\varepsilon_{e\mu}^{uT}, \varepsilon_{e\mu}^{dT})$ (left panel) and $(\varepsilon_{\mu\tau}^{uT}, \varepsilon_{\mu\tau}^{dT})$ (right panel). All GNI parameters are assumed to be real.

VI. CONCLUSIONS

In this work, we studied the potential of two future detectors to constrain non-standard and generalized neutrino interactions via CEνNS measurements at the Spallation Neutron Source. We considered a NaI detector with characteristics similar to the one that is currently being deployed by the COHERENT Collaboration, and a recently proposed cryogenic CsI detector. These detectors have the interesting property that their target materials are composed of nuclei with significantly different proton to neutron

ratios, a feature that is known to be useful for breaking degeneracies among NSI parameters. In addition, they will benefit from a larger statistics than the current CsI detector. We showed that these properties of the future NaI and Cryo-CsI detectors make a combined analysis of their data particularly efficient at breaking degeneracies involving flavor-diagonal NSI parameters, thus strongly improving the current COHERENT constraints on non-standard neutrino interactions. By contrast, no significant improvement is expected for neutrino interactions whose contribution to the CEνNS cross section does not interfere with the SM one

(flavor off diagonal NSIs, scalar and tensor generalized neutrino interactions), unless an important statistical increase is achieved.

ACKNOWLEDGMENTS

[1] D. Z. Freedman, Coherent effects of a weak neutral current, Phys. Rev. D **9**, 1389 (1974).

[2] D. Akimov *et al.* (COHERENT Collaboration), Observation of coherent elastic neutrino-nucleus scattering, Science **357**, 1123 (2017).

[3] D. Akimov *et al.*, Measurement of the coherent elastic neutrino-nucleus scattering cross section on CsI by COHERENT, Phys. Rev. Lett. **129**, 081801 (2022).

[4] D. Akimov *et al.* (COHERENT Collaboration), First measurement of coherent elastic neutrino-nucleus scattering on argon, Phys. Rev. Lett. **126**, 012002 (2021).

[5] M. Cadeddu, N. Cargioli, F. Dordei, C. Giunti, Y. F. Li, E. Picciau, C. A. Ternes, and Y. Y. Zhang, New insights into nuclear physics and weak mixing angle using electroweak probes, Phys. Rev. C **104**, 065502 (2021).

[6] M. Cadeddu, C. Giunti, Y. Li, and Y. Zhang, Average CsI neutron density distribution from COHERENT data, Phys. Rev. Lett. **120**, 072501 (2018).

[7] O. Miranda, D. Papoulias, G. Sanchez Garcia, O. Sanders, M. Tórtola, and J. Valle, Implications of the first detection of coherent elastic neutrino-nucleus scattering (CEvNS) with Liquid Argon, J. High Energy Phys. 05 (2020) 130.

[8] J. Barranco, O. G. Miranda, and T. I. Rashba, Probing new physics with coherent neutrino scattering off nuclei, J. High Energy Phys. 12 (2005) 021.

[9] K. Scholberg, Prospects for measuring coherent neutrino-nucleus elastic scattering at a stopped-pion neutrino source, Phys. Rev. D **73**, 033005 (2006).

[10] V. De Romeri, O. G. Miranda, D. K. Papoulias, G. Sanchez Garcia, M. Tórtola, and J. W. F. Valle, Physics implications of a combined analysis of COHERENT CsI and LAr data, J. High Energy Phys. 04 (2023) 035.

[11] V. Bresó-Pla, A. Falkowski, M. González-Alonso, and K. Monsálvez-Pozo, EFT analysis of new physics at COHERENT, J. High Energy Phys. 05 (2023) 074.

[12] W. Altmannshofer, M. Tammaro, and J. Zupan, Non-standard neutrino interactions and low energy experiments, J. High Energy Phys. 09 (2019) 083; 11 (2021) 113(E).

[13] D. Aristizabal Sierra, V. De Romeri, and N. Rojas, COHERENT analysis of neutrino generalized interactions, Phys. Rev. D **98**, 075018 (2018).

[14] L. J. Flores, N. Nath, and E. Peinado, Non-standard neutrino interactions in U(1)' model after COHERENT data, J. High Energy Phys. 06 (2020) 045.

[15] T. Han, J. Liao, H. Liu, and D. Marfatia, Scalar and tensor neutrino interactions, J. High Energy Phys. 07 (2020) 207.

[16] M. Cadeddu, F. Dordei, C. Giunti, Y. F. Li, and Y. Y. Zhang, Neutrino, electroweak, and nuclear physics from COHERENT elastic neutrino-nucleus scattering with refined quenching factor, Phys. Rev. D **101**, 033004 (2020).

[17] O. G. Miranda, D. K. Papoulias, M. Tórtola, and J. W. F. Valle, Probing neutrino transition magnetic moments with coherent elastic neutrino-nucleus scattering, J. High Energy Phys. 07 (2019) 103.

[18] M. Cadeddu, F. Dordei, C. Giunti, Y. F. Li, E. Picciau, and Y. Y. Zhang, Physics results from the first coherent observation of coherent elastic neutrino-nucleus scattering in argon and their combination with cesium-iodide data, Phys. Rev. D **102**, 015030 (2020).

[19] Y. Farzan, M. Lindner, W. Rodejohann, and X.-J. Xu, Probing neutrino coupling to a light scalar with coherent neutrino scattering, J. High Energy Phys. 05 (2018) 066.

[20] L. M. G. de la Vega, L. J. Flores, N. Nath, and E. Peinado, Complementarity between dark matter direct searches and CEvNS experiments in U(1)' models, J. High Energy Phys. 09 (2021) 146.

[21] E. Bertuzzo, G. Grilli di Cortona, and L. M. D. Ramos, Probing light vector mediators with coherent scattering at future facilities, J. High Energy Phys. 06 (2022) 075.

[22] P. B. Denton and J. Gehrlein, New constraints on the dark side of non-standard interactions from reactor neutrino scattering data, Phys. Rev. D **106**, 015022 (2022).

[23] B. Dutta, Y. Gao, R. Mahapatra, N. Mirabolfathi, L. E. Strigari, and J. W. Walker, Sensitivity to oscillation with a sterile fourth generation neutrino from ultra-low threshold neutrino-nucleus coherent scattering, Phys. Rev. D **94**, 093002 (2016).

[24] T. S. Kosmas, D. K. Papoulias, M. Tortola, and J. W. F. Valle, Probing light sterile neutrino signatures at reactor and Spallation Neutron Source neutrino experiments, Phys. Rev. D **96**, 063013 (2017).

[25] D. Akimov *et al.*, The coherent experimental program, in *Snowmass 2021* (2022), 4, arXiv:2204.04575.

[26] D. Baxter *et al.*, coherent elastic neutrino-nucleus scattering at the European spallation source, J. High Energy Phys. 02 (2020) 123.

[27] A. A. Aguilar-Arevalo *et al.* (CCM Collaboration), First dark matter search results from coherent CAPTAIN-Mills, Phys. Rev. D **106**, 012001 (2022).

[28] H. Bonet *et al.* (CONUS Collaboration), Novel constraints on neutrino physics beyond the standard model from the CONUS experiment, J. High Energy Phys. 05 (2022) 085.

[29] A. Aguilar-Arevalo *et al.* (CONNIE Collaboration), Results of the engineering run of the coherent neutrino nucleus interaction experiment (CONNIE), J. Instrum. **11**, P07024 (2016).

[30] I. Alekseev *et al.* (νGEN Collaboration), First results of the νGEN experiment on coherent elastic neutrino-nucleus scattering, Phys. Rev. D **106**, L051101 (2022).

[31] D. Y. Akimov, I. Alexandrov, R. Alyev, V. Belov, A. Bolozdynya, A. Etenko, A. Galavanov, E. Glagovsky, Y. Gusakov, A. Khromov *et al.*, The RED-100 experiment, J. Instrum. **17**, T11011 (2022).

[32] B. C. Canas, E. A. Garces, O. G. Miranda, A. Parada, and G. Sanchez Garcia, Interplay between nonstandard and nuclear constraints in coherent elastic neutrino-nucleus scattering experiments, Phys. Rev. D **101**, 035012 (2020).

[33] R. R. Rossi, G. Sanchez Garcia, and M. Tórtola, Probing nuclear properties and neutrino physics with current and future CEνNS experiments, Phys. Rev. D **109**, 095044 (2024).

[34] M. Lindner, W. Rodejohann, and X.-J. Xu, Coherent neutrino-nucleus scattering and new neutrino interactions, J. High Energy Phys. 03 (2017) 097.

[35] T. Ohlsson, Status of non-standard neutrino interactions, Rep. Prog. Phys. **76**, 044201 (2013).

[36] O. G. Miranda and H. Nunokawa, Non standard neutrino interactions: Current status and future prospects, New J. Phys. **17**, 095002 (2015).

[37] Y. Farzan and M. Tortola, Neutrino oscillations and nonstandard interactions, Front. Phys. **6**, 10 (2018).

[38] O. G. Miranda, M. A. Tortola, and J. W. F. Valle, Are solar neutrino oscillations robust?, J. High Energy Phys. 10 (2006) 008.

[39] P. Coloma and T. Schwetz, Generalized mass ordering degeneracy in neutrino oscillation experiments, Phys. Rev. D **94**, 055005 (2016); **95**, 079903(E) (2017).

[40] A. Galindo-Uribarri, O. G. Miranda, and G. S. Garcia, Novel approach for the study of coherent elastic neutrino-nucleus scattering, Phys. Rev. D **105**, 033001 (2022).

[41] S. S. Chatterjee, S. Lavignac, O. G. Miranda, and G. Sanchez Garcia, Constraining nonstandard interactions with coherent elastic neutrino-nucleus scattering at the European Spallation Source, Phys. Rev. D **107**, 055019 (2023).

[42] S. C. Hedges, Low energy neutrino-nucleus interactions at the spallation neutron source, Ph.D. thesis, Duke University, 2021, https://hdl.handle.net/10161/24413.

[43] D. Cintas *et al.*, A measurement of the sodium and iodine scintillation quenching factors across multiple NaI(Tl) detectors to identify systematics, Phys. Rev. C **110**, 014613 (2024).

[44] P. S. Barbeau *et al.* (COHERENT Collaboration), Accessing new physics with an undoped, cryogenic CsI CEvNS detector for coherent at the SNS, Phys. Rev. D **109**, 092005 (2024).

[45] O. Tomalak, P. Machado, V. Pandey, and R. Plestid, Flavor-dependent radiative corrections in coherent elastic neutrino-nucleus scattering, J. High Energy Phys. 02 (2021) 097.

[46] J. D. Lewin and P. F. Smith, Review of mathematics, numerical factors, and corrections for dark matter experiments based on elastic nuclear recoil, Astropart. Phys. **6**, 87 (1996).

[47] J. Erler and R. Ferro-Hernández, Weak mixing angle in the Thomson limit, J. High Energy Phys. 03 (2018) 196.

[48] R. L. Workman *et al.* (Particle Data Group Collaboration), Review of particle physics, Prog. Theor. Exp. Phys. **2022**, 083C01 (2022).

[49] S. R. Klein and J. Nystrand, Exclusive vector meson production in relativistic heavy ion collisions, Phys. Rev. C **60**, 014903 (1999).

[50] C. Giunti, General COHERENT constraints on neutrino nonstandard interactions, Phys. Rev. D **101**, 035039 (2020).

[51] O. G. Miranda, G. Sanchez Garcia, and O. Sanders, Coherent elastic neutrino-nucleus scattering as a precision test for the Standard Model and beyond: The coherent proposal case, Adv. High Energy Phys. **2019**, 3902819 (2019).

[52] E. E. Jenkins, A. V. Manohar, and P. Stoffer, Low-energy effective field theory below the electroweak scale: Operators and matching, J. High Energy Phys. 03 (2018) 016.

[53] I. Bischer and W. Rodejohann, General neutrino interactions at the DUNE near detector, Phys. Rev. D **99**, 036006 (2019).

[54] M. Hoferichter, J. Ruiz de Elvira, B. Kubis, and U.-G. Meißner, High-precision determination of the pion-nucleon σ term from Roy-Steiner equations, Phys. Rev. Lett. **115**, 092301 (2015).

[55] T. Bhattacharya, V. Cirigliano, S. Cohen, R. Gupta, H.-W. Lin, and B. Yoon, Axial, scalar and tensor charges of the nucleon from $2 + 1 + 1$-flavor lattice QCD, Phys. Rev. D **94**, 054508 (2016).

[56] L. J. Flores, N. Nath, and E. Peinado, CEνNS as a probe of flavored generalized neutrino interactions, Phys. Rev. D **105**, 055010 (2022).

[57] A. Majumdar, D. K. Papoulias, R. Srivastava, and J. W. F. Valle, Physics implications of recent Dresden-II reactor data, Phys. Rev. D **106**, 093010 (2022).

[58] E. Picciau, Low-energy signatures in DarkSide-50 experiment and neutrino scattering processes, Ph.D. thesis, Cagliari University, 2022.

[59] D. Akimov *et al.* (COHERENT Collaboration), Simulating the neutrino flux from the spallation neutron source for the COHERENT experiment, Phys. Rev. D **106**, 032003 (2022).

[60] S. C. Hedges, The NaI[Tl] COHERENT detector, *Talk at the Magnificent CEνNS Workshop* (2018), 10.5281/zenodo.3462345.

[61] K. Ding, Development of cryogenic scintillation detectors for the search of new physics, Ph.D. thesis, The University of South Dakota, 2024, https://www.proquest.com/dissertations-theses/development-cryogenic-scintillation-detectors/docview/3051297331/se-2.